NTNU

Norwegian University of
Science and Technology

Modeling and Control of a DC-grid Hybrid Power System with Battery and Variable Speed Diesel Generators

Tron Hansen Syverud

Master of Energy and Environmental Engineering
Submission date: June 2016
Supervisor: Roy Nilsen, ELKRAFT

Norwegian University of Science and Technology
Department of Electric Power Engineering

Acknowledgments

I would like to thank my supervisor Roy Nilsen for his support and patience answering all my questions throughout the work of this master thesis. His experience from marine power industry has helped me lifting the quality and relevance of this thesis. My deepest thanks, also go to all the students in the Energy and Environmental Engineering study program at NTNU. So much joy and motivation have been brought to me because of you.

Abstract

Hybrid electric power systems (HPS) have successfully been integrated in the road-traffic industry due to enhanced efficiency and environmental benefits. Recently this concept has been implemented in the marine sector. In this master thesis, the construction of a DC hybrid power system for a marine vessel is outlined in detail. The HPS is developed in Matlbat/Simulink and comprises two set of diesel generators with variable speed, six-pulse diode bridges, a battery bank, bidirectional converter and a constant power load (CPL). The associated controllers which are designed includes battery controller, engine speed controller and voltage-exciter controllers. An emphasized focus will lay on structures of voltage-exciter controllers. For this purpose, control structures for operation of generator set alone or together with the battery are investigated. The performance of all controllers are tested for a specific test-bench. In addition to this, specific fuel-oil consumption (SFOC) of the diesel engine will be evaluated through an implemented SFOC-model, where SFOC for operation both with and without battery is compared.

Table of Contents

List of Tables

List of Figures

Nomenclature

Acronyms

AC	Alternative current
CPL	Constant power load
DC	Direct current
DOH	Degree of hybridization
ESD	Energy storage devices
HPS	Hybrid power system
IGBT	Insulated gate bipolar transistor
Li-ion	Lithium ion
PI	Proportional-integral
PID	Proportional-integral-derivative
PM	Phase margin
pu	per unit
PWM	Pulse width modulation
R&D	Research and development
RMS	Root mean square
SFOC	Specific fuel oil consumption
SOC	State of charge

Parameters

δ	Slope of droop controller
τ	Time delay in diesel engine
τ_c	Time constant in diesel engine
τ_{ex}	Time constant of exciter machine
C	Filtering capacitor in the DC-link

C_r	Mechanical loss coefficient
C_{in}	Capacitor of low-voltage side of converter
C_{out}	Capacitor of high-voltage side of converter
d	Duty ratio signal to PWM
f_s	Switching frequency
I_{DC}	DC-current of generator set
J_{eq}	Equivalent intertia
K_p	Control gain
K_y	Torque constant of diesel engine
K_{pi}	Control gain of an inner control-loop
K_{po}	Control gain of an outer control-loop
L	Inductor in bidirectional converter
L''_d	Subtranisent inductance of d-axis in synchronous generator
L_k	Commutation inductance
L''_q	Subtranisent inductance of q-axis in synchronous generator
R_k	Commutation resistance
R_L	Resistance of inductor
T_i	Integral time constant in controller
T_m	Mechanical torque
T_{Bat}	Time constant in battery droop controller
T'_{d0}	Transient time constant in synchronous generator
T_{di}	Filtering time constant of speed reference
T_{el}	Electrical torque
T_{eq}	Equivalent time constant
T_{filt}	Filtering time constant of a measurement
T_{ii}	Integral time constant of an inner-controller
T_{io}	Integral time constant of an outer-controller
$T_{m,max}$	Maximum torque develompment of diesel engine

T_{MS}	Time constant in current controller of generator
T_{sum}	Sum of time constants
T_{sw}	Time delay in PWM
V_0	Idle voltage at no-load in droop controller
V_{Bat}	Battery voltage
β	Adjustable factor in symmetrical optimum
ω_m	Mechanical speed in rad/s
H	Inertia time constant
N	Numbers of cylinders in diesel engine
n_m	Mechanical speed
p	Poles in synchronous generator
P_{Bat}	Output power of battery
P_{gen}	Output power generator
R_{CPL}	Constant power load resistance
R_{on}	Switching resistance in IGBT
v_f	Field voltage input to generator
V_{DC}	DC-link voltage
Y	Fuel injection
*	Denotes a reference signal
n	Subscript denoting a nominal value

1 | Introduction

World-wide concerns of global warming and emissions of toxic chemicals have increased the demand for environmentally friendly energy solution. In the maritime sector, the International Maritime organization has through MARPOL [1] imposed regulations on ships to reduce emissions of NOx and SOx and given requirements of a minimum efficiency level for ships transporting goods [1]. This has opened up hybrid propulsion systems as an attractive solution. Hybrid propulsion systems are successfully being established in the vehicle industry, but in the marine sector it is still in its initial start up. However, recently built hybrid ships have proven to be beneficial. The hybrid vessel Viking Lady, built in 2009, have estimated cut of CO_2-emissions up to 50 % and up to 30 % improvement of energy efficiency compared to a conventional power system [2]. The electrical ferry Ampera has reported fuel savings of 60 % per year which gives an estimated investment payback of four years compared with a compustion propulsion system [3].

In the realization of hybrid power systems, a transition of DC to AC-power system is initiated. Compared to a shipboard AC-grid, DC-grid allows for more flexibility as diesel generator sets are not locked to operate at fixed speed. This attributes less fuel consumption as the diesel engine can operate at optimal speed for maximized efficiency. A DC-system furthermore is flexible in combining other energy sources such as fuel cells, solar power and energy storage devices. Lastly a DC-grid has lower electrical footprint and more flexible placement of components than the AC-grid, which gives more space for payload [4].

In this transition from a traditional AC-power system to a DC HPS, new control structures and energy managements strategies for healthy operation of energy units must be developed. In this context, control strategies addressed for microgrids as master-slave and droop control are applicable [5]. And what still is a relevant topic, either in land-based microgrids, hybrid vehicles or marine HPS, are effective controllers that provide minor computation and communication, reliability and high energy efficiency [6] [7] [8].

1. International Convention for the Prevention of Pollution from Ships

1.1 Objectives

This master thesis will seek to address and show principles concerning the following objectives

- Model a simulation platform of a DC-grid hybrid power system composing of diesel-generators, battery storage system and constant power load.
- Develop and test performance of associated control structures including speed controller of diesel engine, voltage-exciter controllers and battery converter controller.
- Show applications of the developed power system trough a driving profile and assess performance with respect to fuel consumption.

1.2 Limitations

Parameters used to model the diesel-generator set and exciter-system are not corresponding to a real existing system. They rather are acquired based on what is meant to be realistic parameters. Moreover simulation results are obtained using discrete solver in Simulink. This can in particular give misleading and inaccurate results at transients, for example in the size of resulting over-voltage when load is disconnected.

2 | Background

2.1 Hybrid power systems

In the context of a hybrid power systems, the term hybrid refers to the fact that a share of power is supplied by batteries in addition to diesel power. The two-stroke diesel engine is the most frequently applied prime mover in the marine industry [9]. Likewise for hybrid electrical vehicles, types of shipboard hybrid systems can be divided into the following three types [10]:

- Hybrid electric ships (HES)
- Plug-in hybrid ships (PHES)]
- Full-electric ships (FES)

HES have hybrid power systems where energy storage devices usually are used to increase the performance of the diesel engine for reduction of fuel consumption. PHES is similar to HES, but feature the possibility to charge batteries on shore. For ships spending a great deal of time at harbor, this is a convenient solution as diesel engines can be turned off and batteries supply all propulsion to the ship. Charging battery with land-power will be a cost effective solution in case of low electricity price. Turning off diesel engines, also has a positive effect on the local air quality. On a FES, all power is solely supplied by batteries. FES can typically be employed for shorter ferry routes where access to charge power is situated nearby. An example of this is the Siemens produced ferry Ampere [3].

2.2 Fuel savings

Diesel engines have an optimal operation load point, at which it will display lowest fuel consumption. During a voyage, load points of the diesel engine will typically not be at optimum. This is illustrated in figure 2.1, which depicts the operating load point of a vessel over a time interval of one month. The blue line indicates the optimal operating point. Introducing batteries to the shipboard power system, the power supplied by diesel generators can be controlled to stay at the optimal point. The battery, will in this case absorb or supply the excess power and power lack respectively. In this regard, a battery configuration displays an efficiency up to 99 % [11].

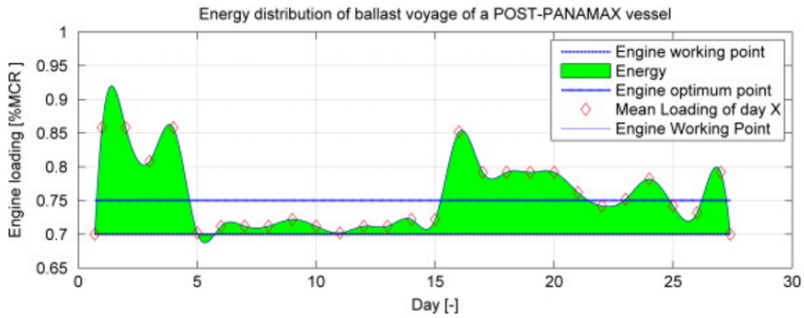

Figure 2.1: *Load points of a vessel during a voyage of one moth. The blue line represents the optimal operating point. MCR=Maximum contineous rating. Source: [9]*

Besides having an optimal load point, diesel engines also have an optimal speed for any load point. As DC-power distribution does not lock the diesel generator to operate at fixed speed, the engine speed can be optimized with respect to load. In figure 2.2 typical specific fuel oil consumption [gr/kWH] (SFOC) with respect to load and engine speed is plotted. This figure shows that with fixed speed at 1000 *rpm* the fuel consumption will be notable increased at low load. The line showing variable speed operation aim to track the optimal speed level for each load.

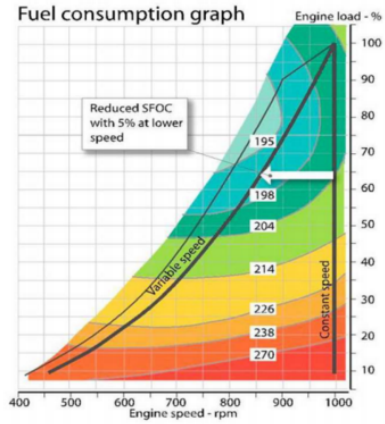

Figure 2.2: *Specific fuel oil consumption [gr/kWH] with respect to load and engine speed. Source: [12]*

Moreover, it is observed that diesel engines display higher fuel consumption at transient operation when load and speed are varying [13]. Unfortunately, not much research is found available on this topic, which is an important aspect regarding variable speed operation. However, this observation is an other advantage of installing a battery pack, as power supplied by the generator set will tend to be more steady.

2.3 Batteries

Batteries are energy storage devices with large energy capacity and is the most widespread technology for energy storage in HPS. Battery packs represent an expensive unit in the HPS and healthy operation for prolonged life time is intrinsic. Batteries, such as Li-ion batteries should be neither fully charged nor discharged [14]. The number of discharge cycles a battery can sustain before performance is notable decayed is called cycle-life. Avoiding operation with high C-rates, will also have positive effects of the battery performance. C-rate is defined as the current causing a fully charged battery, being discharged in one hour, i.e. a battery of $1Ah$ has a C-rate of $1\,A$ [15]. Moreover the ambient temperature is of particular importance for battery performance as well as degradation. Low temperature operation will reduce reaction rate in the battery and thus limit power flow. Operation at high temperatures will boost up reaction rate, but simultaneously also lead to increase of parasitic side reactions which contribute to degradation of the battery [16]. Overheating of a battery may in worst case lead to thermal run-away. This phenomena involves a chain of stages which includes breakdown of layers between anode, electrolyte and cathode. The effect of this are chemical reactions that release flammable gases and increase pressure, which in turn can result in fire and explosion [17]. To keep battery systems in healthy operating states, a battery management system monitors and controls important battery parameters such as temperature, state of charge, voltage and cell balance [18] [19].

2.3.1 Battery types and applications

Among several types of batteries, Li-ion batteries have been found most attractive in HPSs due to properties such as high energy density, long cycle life and low self-discharge rate [6] [20]. Li-ion batteries are, however, the most costly, but are expected further to decrease due to diffusion of hybrid vehicles [21]. Li-ion batteries represents a series of battery chemistries, where each type is associated with individual advantages and disadvantages. Table 2.1 shows performance of selected properties for the batteries Li-ion batteries LTO, LFP, LMO, NMC and NCA (see table for acronyms).

According to table 2.1, the battery types display varying performance of the selected properties. NCA has highest energy density, but low C-rate and cycle life. HEV-manufacturers, such as Tesla that uses NCA, often tend to oversize the battery pack to compensate for the low C-rate and thus decrease charging time [22]. Oversizing the battery also has positive effect on the life span as cycles will be less deep. Batteries can be combined together to benefit from their individual properties. In Nissan Leaf, LMO is mixed with NMC for increasing energy capacity and life time [23].

	LTO	LFP	LMO	NMC	NCA
Cell voltage [V]	2.4	3.2-3.3	3.7-3.8	3.6-3.7	3.6
Energy density [Wh/kg]	70-80	90-120	100-150	150-220	200-260
Charge [C-rate]	1-5	1-3.65	0.7-3	0.7-1	0.7
Discharge [C-rate]	10	1-25	1-10	1-2	1
Cycle life	3000-7000	1000-2000	300-700	1000-2000	500
Thermal runaway [$C°$]	Very safe	270	250	210	150
Price	Very high	Moderate	Moderate	Moderate	High

Table 2.1: *Properties of selected Li-ion batteries. LTO=Li-titanate, LFP=Li-phosphate, LMO=Li-manganese, NMC=Li-nickel-manganese-cobalt, NCA=Li- nickel-cobalt-aluminum-oxide. Source: [23]*

Compared to applications in hybrid electric vehicles (HEV), battery packs employed for marine applications may be hundred times larger and subjected to tough load profiles that causes much stress on the battery [10]. Reliability and safety of batteries are therefore properties of high importance on shipboard power systems. Among the Li-ion batteries in table 2.1, LTO and LFP are considered the safest batteries due to high thermal run-away temperature [23]. LTO and LPF also appears to be the batteries with highest C-rate and high cycle life. These are properties that make them suitable for high power applications such as blackout prevention and fast charging. Among recently built hybrid electrical ships, i.e Viking Lady, a battery pack of NMC is installed [24]. This is a battery type with high energy density and good cycle life.

A field of attention in R&D of the battery technology is the use of silicon as anode material instead of graphite which is the standard of conventional Li-ion-batteries. The theoretical capacity of using silicon is $4200 mAh/g$ which is almost ten-folds of the capacity with anodes made of graphite. However, due to large volume expansion of silicon in the electrochemical process, cycle life is limited. To overcome this challenge, nano-structures of silicon is in development [25].

2.4 Recent research on hybrid power systems

Much research has been done on the field hybrid power systems. A great amount of this is addressed HEV. And much of this research can be applied to hybrid hybrid electric ships. Of researching and information directly addressing hybrid electric ships, advantages of hybrid power systems are well documented through operational data of ships [9]. The doctoral thesis in [26] gives a comprehensive study of DC-grid hybrid power systems combining battery and diesel generators. This study presents the building blocks required to obtain a simulation model. It also assesses optimization strategies for reduced fuel consumption. Developed models of generator sets and battery in this study are, however, obtained using averaging techniques where the effect of ripple current are not

present. Details around implementation of control systems of diesel generators are also not included. Average models often are precise in predicting stationary operation, but tend to be inaccurate for transient operation [27]. In this thesis control structures and operation of HPS will be investigated through detailed models.

3 | Modeling of hybrid power system

A HPS has been built up and simulated in Matlab/Simulink using the SimPowerSystem toolbox. Implemented sub-models which will be presented in this chapter, comprise two diesel-generator sets, a six-pulse diode bridge rectifier, a battery and a constant power load (CPL).

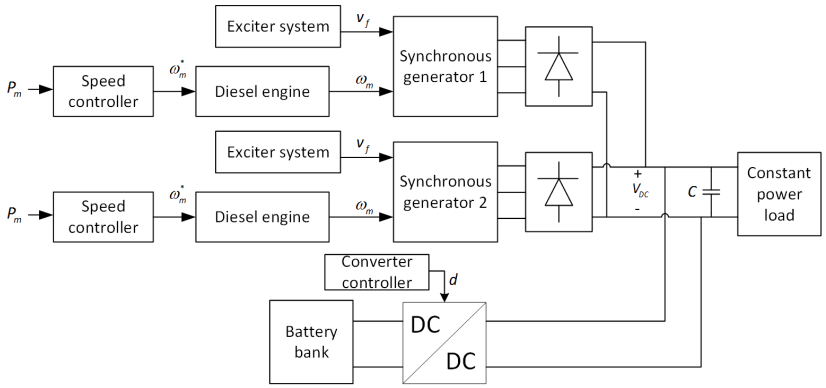

Figure 3.1: *Block diagram of the modeled hybrid power system*

3.1 Requirements of hybrid power system

3.1.1 Sizing of generator set and battery bank

In the modeled HPS, actual load data from a dynamic position situation with two generators are used for dimensioning the HPS [28]. The total load demand is depicted in figure 3.2.

In the context of dimensioning of a HPS, the term degree of hybridization (DOH) is often referred to. One definition of DOH is the ratio of battery power and the total installed power [29]. It is possible to dimension the DOH to yield optimal performance of key parameters for HPSs combining a power generating set and an energy storage system. In [30] a cost-function based strategy is developed to optimize the DOH in a hybrid vehicle with aspect to fuel economy, emissions and vehicle performance.

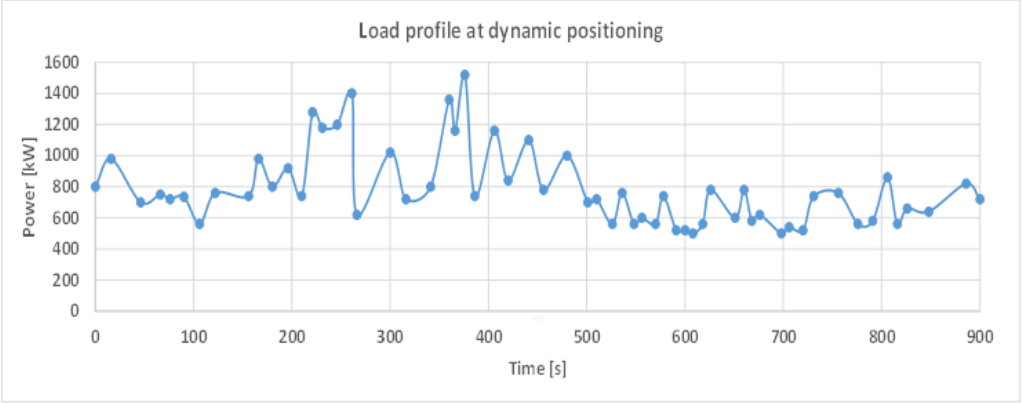

Figure 3.2: *Total power supplied by two generator sets during dynamic positioning. This load profile is used for dimensioning of the HPS*

Considering the load profile in figure 3.2 an optimal DOH could be obtained according to equation 3.1 [29]. In this case, the generator set would be dimensioned to yield at the time-averaged P_{avg} given in equation 3.2. Using the trapezoidal integral method to calculate P_{avg}, equation 3.1 yields $DOH_{opt} = 0.48$ with $P_{avg} = 787\,kW$ and $P_{max} = 1520\,kW$. Furthermore when using battery power, the battery must be dimensioned to store sufficient energy for avoiding being completely discharged or overcharged for the dimensioning driving cycle. For this purpose, there are many techniques to balance state of charge of the battery within healthy limits [7]. On a vessel with several generator sets, generator sets can be turned on and off depending on SOC of the battery.

$$DOH_{opt} = \frac{P_{max} - P_{avg}}{P_{max}} \tag{3.1}$$

Where

$$P_{avg} = \frac{\int_0^t P_{load}(t)}{t} \tag{3.2}$$

In this thesis, as simulation cases with generator sets operating alone will be considered, the generator set is dimensioned to supply the maximum load. In table 3.1 dimensioning requirements of the HPS is summarized. The battery power level of $P_{Bat} = 800kW$ will be sufficient to supply the highest power peak while the generator sets supply average power. The DC-link voltage $V_{DC} = 930\,V$ is chosen based on the average DC-voltage resulting from a generator with $V_{ll,RMS} = 690\,V$. This is further explained in section 3.2.1.

$P_{Gen,1}$	$P_{Gen,2}$	P_{Bat}	V_{DC}
$800\,kW$	$800\,kW$	$800\,kW$	$930\,V$

Table 3.1: *Dimensioning parameters of the modeled HPS*

3.1.2 Modeling of load

The main load in a ship is the thrusters which are connected to an electrical drive system comprising DC/AC-inverters and electrical motors. Such drive systems display a constant power load-characteristic since it is able to draw the same amount power for any voltage. This behavior is due to the choppers that will adapt the switching time in order to draw the required power. To model a constant power load (CPL) in Simulink, a controlled current source can be used where the demanded current is obtained by dividing a reference power by the actual DC-link voltage as shown in equation 3.3.

$$I_{load} = \frac{P_{ref}}{V_{DC}} \tag{3.3}$$

The linearized expression of a CPL is given by equation 3.4 [31]. v denotes small voltage perturbations.

$$i = -\frac{P}{V^2}v + 2\frac{P}{V} \tag{3.4}$$

At a given operating point, CPL then can be represented by a negative resistance parallel with a constant power given in equation 3.5 and 3.6. The negative increment of the resistance has a destabilizing effect on a power system and is known as negative impedance instability [32].

$$R_{CPL} = -\frac{V^2}{P} \tag{3.5}$$

$$I_{CPL} = 2\frac{P}{V} \tag{3.6}$$

3.1.3 Test bench of controllers

In this thesis several controllers will be designed. To test the performance of the controllers, they will be subjected to a test bench similar to industrial standards. The test bench consists of load increments of $\frac{1}{3}pu$ of full load and finally a drop to no load as shown in figure 3.3. Of particular interest is how controllers perform from full load to no load. The increment of load of thrusters can be controlled to proceed smoothly whereas a drop out of load can be harmful and cause over voltage. The drop from full load to no load will, thus, be the worst case scenario.

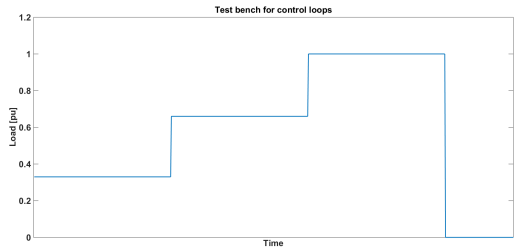

Figure 3.3: *Test bench which will be used to test performance of controllers.*

3.2 Synchronous generator

A model of a synchronous generator with quantities of inductances given in per-unit is provided from the Simulink library [33]. The model is based on the equations 3.7-3.16. The generator takes the pu-values of field voltage v_f and the engine speed ω_m as input. The transformation of pu-values and real values is given in appendix section A.2.

$$\lambda_d = L_d i_d + L_{ad} i_D + L_{ad} i_f \tag{3.7}$$
$$\lambda_q = L_q i_q + L_{aq} i_q \tag{3.8}$$
$$\lambda_D = L_D i_D + L_{ad} i_d + L_{ad} i_f \tag{3.9}$$
$$\lambda_Q = L_Q I_Q + L_{aq} i_q \tag{3.10}$$
$$\lambda_f = L_f i_f + L_{ad} i_d + L_{ad} i_D \tag{3.11}$$

$$v_d = R_s i_d + \frac{d}{dt}\lambda_d - \omega_{el}\lambda_q \tag{3.12}$$
$$v_q = R_s i_q + \frac{d}{dt}\lambda_q + \omega_{el}\lambda_d \tag{3.13}$$
$$v_D = R_d i_d + \frac{d}{dt}\lambda_d \tag{3.14}$$
$$v_Q = R_Q i_Q + \frac{d}{dt}\lambda_q \tag{3.15}$$
$$v_f = R_f i_f + \frac{d}{dt}\lambda_f \tag{3.16}$$

Number of poles are chosen in order to cause no gear on the shaft between the diesel engine and the generator. This is obtained when the rated mechanical speed of the generator is equal to the rated engine speed.The relationship between electric speed and mechanical speed ω_m is given in equation 3.17. Avoiding gear, will reduce the mechanical looses of the drive train. With a nominal engine speed of 1000 rpm and nominal generator frequency of $\omega_{el} = 50Hz$, number of poles p can be obtained according to equation 3.18-3.20.

$$\omega_{el} = \frac{p}{2}\omega_m \tag{3.17}$$
$$2\pi 50 = \frac{p}{2}\frac{1000 \cdot 2\pi}{60} \tag{3.18}$$
$$100\pi = \frac{p}{2}\frac{100\pi}{3} \tag{3.19}$$
$$\rightarrow p = 6 \tag{3.20}$$

3.2.1 Diode bridge

A six pulse uncontrolled diode bridge rectifier is used to transform the output AC-current from the synchronous generator to DC. 3.4 shows the topology of this configuration. The diode bridge benefits from its simplicity and low cost. However, disadvantages consist in highly production of harmonics. Harmonic content in the voltage and current of an electrical machine increases iron and copper losses. These additional losses may lead to reduced efficiency, pulsations in the developed torque and mechanical damages [34]. In [35], four different rectifier topologies are presented and connected to a permanent-magnet generator. The authors in this study do not take any conclusion to what is the preferable topology. A three-phase PWM-rectifier would produce less total harmonic distortion, but suffers from higher power losses. The diode rectifier has the lowest power losses of the topologies under study.

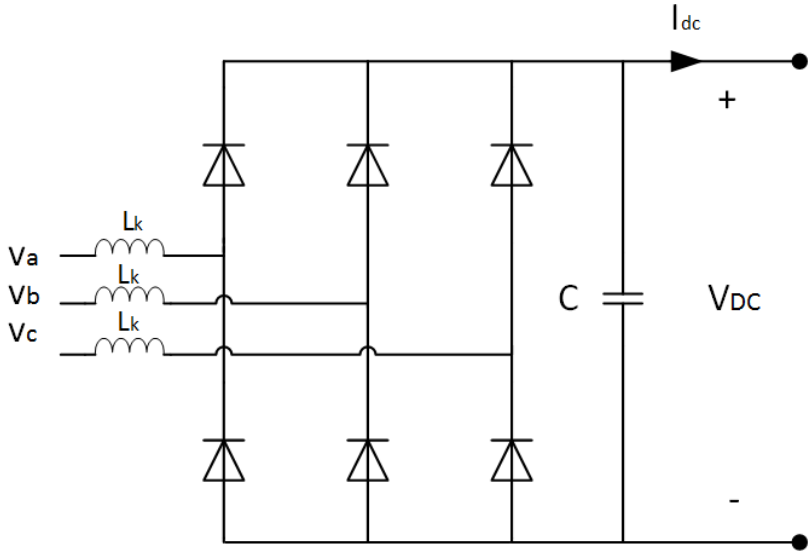

Figure 3.4: *Six-pulse diode rectifier used in the modeled HPS.*

The output DC-link voltage from the diode bridge is given in equation 3.21, where the negative term expresses the voltage drop due to commutation [36, p. 108]. A generator of $V_{LL,RMS} = 690\,V$ results in a maximum voltage at the DC-link of $931.5\,V$. The capacitor at the DC-link smoothen out the DC-link voltage in order to yield small voltage ripple. For the actual system, C is chosen $20mF$.

$$V_{dc} = \frac{3}{\pi}\sqrt{2}V_{LL} - \frac{3}{\pi}\omega_{el}L_k I_{dc} \tag{3.21}$$

The diode-bridge impacts the dynamic behavior of the synchronous generator compared to normal operation in an AC-DC-link. This is due to the commutation between two phases which causes a line-to-line short circuit, with a frequency six times the phase-frequency. During the commutation a commutation inductance, L_k is defined which varies

according to overlapping angle u and also during the commutation. An averaged commutation inductance during a commutation interval can be approximated by equation 3.22 [37].

$$L_k = \frac{L''_d + L''_q}{2} + \frac{L''_d - L''_q}{2} cos(2\phi + u) \tag{3.22}$$

ϕ is the internal phase angle,u commutation overlapping angle and L''_d and L''_q are subtransient reactants. In the range of $2\phi + u$ from $[0, \pi]$, L_k will be between 0.13 and 0.15 pu according to values of L''_d and L''_q given in appendix section A.1. For small values of $2\phi + u$, $L_k \approx L''_d$. Effects of the commutation process, results in distorted sinus-waveforms of output voltage and current as well steady ripples in output power and electromagnetic torque. Waveforms of selected outputs of the generator-diode bridge model is shown in appendix section A.4.

3.2.2 Exciter system and voltage excitation

The exciter system which feeds the field-voltage input to the synchronous generator is assumed composing of a rotating exciter machine. A first-order transfer function with the time-constant τ_{ex} is used to model the exciter machine. The transfer-function from a field-voltage-reference to field voltage input v_f then becomes as shown

$$\frac{v_f}{v_f^*} = \frac{1}{\tau_{ex} s + 1} \tag{3.23}$$

The transfer function from the field voltage input to the terminal voltage can be expressed in terms of per-unit according to equation 3.24 [38, p. 345].

$$\frac{V_t}{v_f}(s) = \frac{1}{1 + T'_{d0}} \tag{3.24}$$

Presenting $\frac{V_t}{v_f}(s)$ as first order transfer-function is a rough approximation which is only valid in steady state with the generator on open circuit. Representing the synchronous machine as a first-order transfer function for control purposes is also reported in other literature [39]. If also including equation 3.23, the control loop from field voltage reference to the phase voltage becomes

$$\frac{v_\phi}{v_f^*}(s) = \frac{1}{\tau_{ex} s + 1} \cdot \frac{1}{1 + T'_{d0}} \tag{3.25}$$

3.2.3 Equivalent DC-circuit

The equivalent DC-circuit representing the synchronous generator, diode and the load is shown in 3.5. This equivalent circuit will be investigated for design of controllers. The resulting commutation inductance at the DC-link will be $2L_k$ since it connects two phases of the generator[40, p. 149]. The commutation voltage drop is represented by $R_k = \frac{3}{\pi}\omega_{el}L_k$.

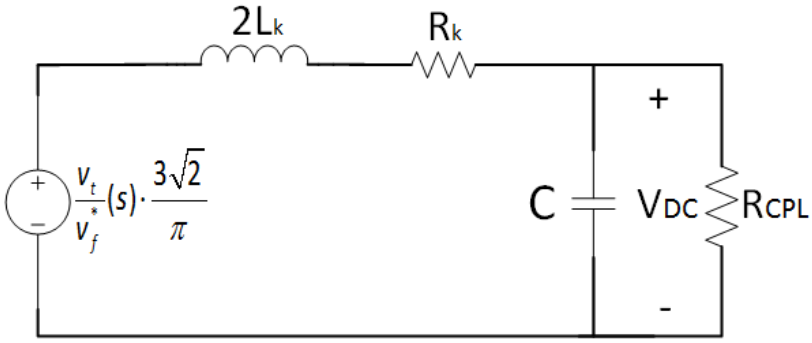

Figure 3.5: *Equivalent DC-circuit of generator set*

3.3 Diesel engine

3.3.1 Model of diesel engine

The dynamic model of a diesel engine used in this thesis is reported in several other studies i.e [41] [42] [43]. The engine-model composes of a governor, engine dynamics and a mechanical system. The model is expressed in terms of per-unit and normalized with respect to pu-values of the generator. To account for losses and overrated output power of the generators, the diesel engine is dimensioned with 10 % higher power ratings than the synchronous generator i.e. $880\,kW$. This is implemented with a maximal output torque of the diesel engine of $1.1\,pu$. The engine speed is equal to mechanical speed of the synchronous generator as explained in section 3.2.

The governor commands the fuel injection $Y(s)$ and is represented by a PI-controller. Due to physical constraints on the torque characteristics of the diesel engine, the fuel index from the governor is limited as a function of measured shaft speed given by equation 3.26, where Y_{max} states maximum fuel injection [43]. Since the diesel engine is rated 10 % higher than the generator, output of Y_{max} is multiplied by 1.1. This gives a maximum torque output of $1.1\,pu$.

$$Y_{max} = 1.1 \left\{ \begin{array}{lll} 0.4 & for & n_m \leq 40\,\%\ of\ n_{rated} \\ 1 & for & n_m \geq 80\,\%\ of\ n_{rated} \\ \frac{1.5 n_m}{n_{rated}} - 0.2 & & otherwise \end{array} \right\} \tag{3.26}$$

The relationship between fuel injection $Y(s)$ and output torque of the engine T_m is described by

$$T_m(s) = e^{-\tau s} \frac{K_y Y(s)}{1 + \tau_c s} \tag{3.27}$$

where K_y is the engine gain. τ_c is the time constant corresponding to torque build-up from cylinder firings given by

$$\tau_c \approx \frac{0.9[rad]}{2\pi n_m[rps]} \tag{3.28}$$

The time constant τ, represents a time delay half the period between consecutive cylinder firings which can be calculated by equation 3.29 [42].

$$\tau \approx \frac{1}{2N n_m[rps]} \tag{3.29}$$

It should be noted that the behavior of the diesel engine will vary depending on the shaft speed. From equation 3.26 maximum output torque will be limited with lower speed. Variations in τ and τ_c impact phase-margin of the control system as will be illustrated in next section.

To express the mechanical system, Newton's second low in terms of angular motion is employed

$$J_{eq} \frac{d\omega_m}{dt} = T_m - T_{el} - \omega_m C_r \tag{3.30}$$

where J_{eq} is the equivalent inertia of the drive train, T_{el} electrical torque and C_r rotational losses coefficient. To express 3.30 in terms of per unit, an inertia constant $H\,[seconds]$ is defined in equation 3.31 [38, p. 128-131].

$$H = \frac{J_{eq}\omega_{base}^2}{2P_{base}} = \frac{J_{eq}\omega_{base}}{2T_{base}} \tag{3.31}$$

By expressing equation 3.30 with J_{eq} replaced by H, the relationship in 3.32 can be obtained, which yields the pu-expression of the mechanical system.

$$\frac{d\omega_{m,pu}}{dt} = \frac{d\omega_m}{dt(\omega_{base})} = \frac{T_m - T_{el} - \omega_{base} C_r}{2HT_{base}} = \frac{T_{m,pu} - T_{m,pu} - \omega_{m,pu} C_r}{2H} \tag{3.32}$$

In the implemented model, the mechanical system is stated in the s-plane according to equation 3.33. Hereafter, pu-subscript will not be added.

$$\omega_m = \frac{T_m - T_m - \omega_m C_r}{2Hs} \tag{3.33}$$

3.3.2 Design of speed controller

The open control loop from reference speed to output speed of the engine is formulated in equation 3.34 where the contribution from the electromagnetic torque and mechanical losses is neglected.

$$\frac{\omega_m}{\omega_m^*}(s) = K_p \frac{1+T_i s}{T_i s} \cdot e^{\tau s} \frac{K_y}{\tau_c s + 1} \cdot \frac{1}{2Hs} \tag{3.34}$$

The governor of the speed engine, which is presented as a PI-controller, is used to control the engine speed. Concerning tuning of the PI-controller, equation 3.34 constitutes a symmetrical optimum case due to the integral $\frac{1}{2Hs}$ (see appendices section A.5). The control parameters for K_p and T_i is tuned based on equation 3.36 and 3.35, which is proposed parameters for this particular process in [44, p. 342]. τ and τ_c are considered, at maximum engine speed $n_m = 1\,pu$ i.e $16.67\,rps$. This speed level yields $\tau = 0.0050\,s$ and $\tau_c = 0.0086\,s$. For enhanced dynamic response of the controller, it is found appropriate to double the value of K_p from equation 3.36. Table 3.2 shows the selected control parameters.

$$T_i = \beta\tau, \quad \beta \approx 20 \tag{3.35}$$

$$K_p = \frac{1}{K_{gain}\tau_c\sqrt{\beta}}, \quad K_{gain} = K_y \frac{1}{2H} \tag{3.36}$$

$T_i = 0.1$	$K_p = 26$

Table 3.2: *Control parameters of speed controller*

Figure 3.6 and figure 3.7 show the open loop and closed loop bode diagram respectively of the speed control loop for the selected speed levels $n_m = 1\,pu$, $n_m = 0.7\,pu$, $n_m = 0.5\,pu$ and $n_m = 0.4\,pu$. As the time constants τ and τ_c increases with lower engine speed, phase margin of the control loop will decrease as well. From a phase margin of 47° at $n_m = 1\,pu$, the phase-margin is below 10° at $n_m = 0.4\,pu$ and the system is almost unstable. This tendency is reflected in the closed loop bode digram shown in figure 3.7. At $n_m = 0.4$ a high peak arises, which indicated poor tracking relationship. With the applied control parameters, it is therefor suggested having a minimum speed of $0.5\,pu$. At this level phase margin is 17.3° which is also very low. In general in control theory, the phase margin should be at least greater than 45°. However, as disturbances in the load torque will be damped through the inertia of the drive train, lower phase margins can be tolerated. For better stability at low speed levels, controller with adaptive parameters could be implemented. This can be achieved by adjusting the value of K_p with respect to engine speed.

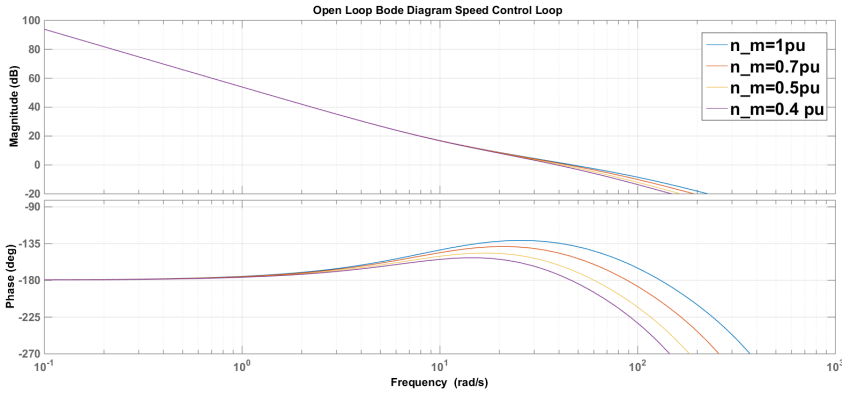

Figure 3.6: *Open loop bode plot of speed control loop for selected engine speed levels. With decreasing speed, phase-margin also decreases.*

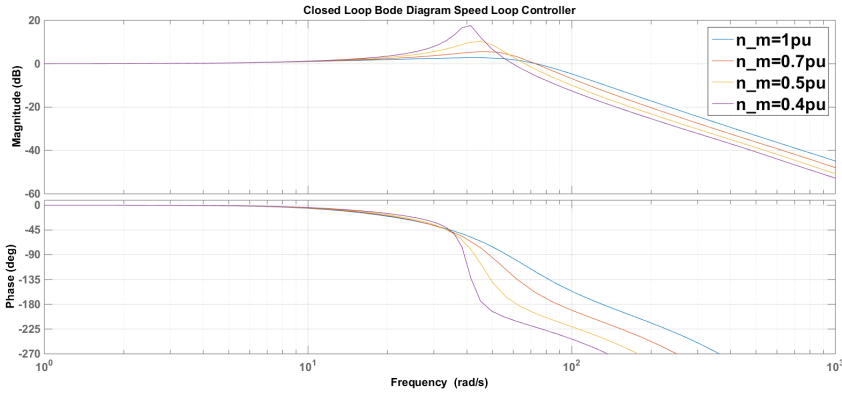

Figure 3.7: *Closed loop bode plot of speed control loop for selected engine speed levels.*

3.3.3 Optimal speed reference

To obtain optimal speed control in terms of minimizing fuel consumption, a lockup table with optimal speed reference with respect to engine power is made. Data for the lockup table are retrieved from figure 2.2, where data points according to the variable speed curve is considered. Interpolation is performed between the data point to have a continuously reference signal. In figure 3.8, the optimal speed reference signal is depicted.

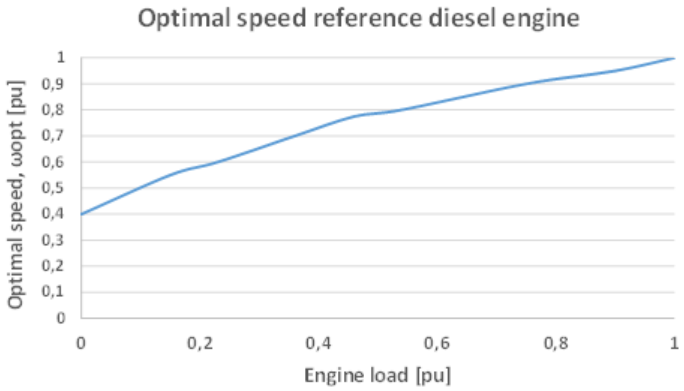

Figure 3.8: *The graph shows plotted optimal speed references for given engine loads. The optimal speed reference is used as input to the speed controller of the diesel engine*

As stated in equation 3.26 the maximum torque of the diesel engine depends on engine speed. In the establishment of an optimal speed reference it is important to make sure that the torque levels corresponding to the optimal speed curve are considerably lower than the maximum torque. Not only is this essential so that the engine can react on a load increase, but also for decent acceleration when speed is increasing. In figure 3.9 the maximum output torque is plotted against the corresponding torque of the optimal speed curve. Actual torque is obtained by $\frac{P_m}{\omega_{opt}}$. Figure 3.9 shows that there is a certain margin between maximum torque and the engine torque. From speed levels above $0.9\,pu$, slower acceleration is indicated as the margin between the curves is smaller.

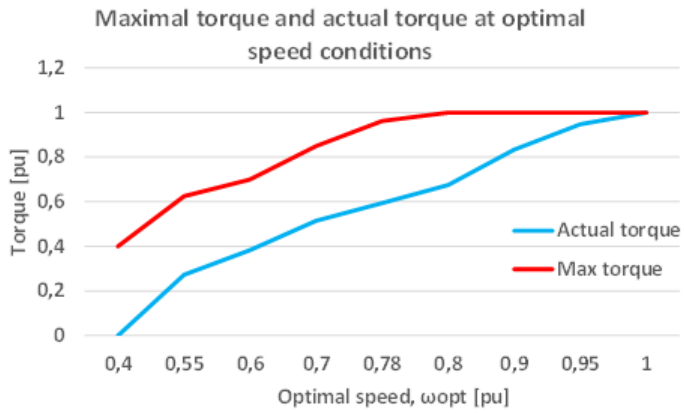

Figure 3.9: *The graph shows maximum possible engine torque and the actual torque corresponding to optimal speed.*

3.3.4 Realization and testing of speed controller with optimal speed reference

In order to include optimal speed control of the speed loop, the engine power is fed into the lockup table which states the speed reference. The engine power is calculated by equation 3.37.

$$P_m = T_m \cdot \omega_m \tag{3.37}$$

A stability issue arises as the reference speed changes according to output power of the engine. Thus, the speed reference forms an outer loop that needs to be slower than the speed control-loop. The engine power is therefore filtered, through a first order low-pass filter on the form

$$H(s) = \frac{1}{sT_{di} + 1} \tag{3.38}$$

where T_{di} is the cutoff time constant. Stability of the engine speed, is obtained when $\frac{1}{T_{di,c}}$ is at least one decade lower than the lowest crossover frequency $\omega_{c,min}$ i.e. $41.3\,rad/s$. Thus, T_{di} is stated according to equation 3.39. The block diagram of the speed-loop is depicted in figure 3.10.

$$T_{di} > \frac{1}{\omega_{c,sl}/10} \tag{3.39}$$

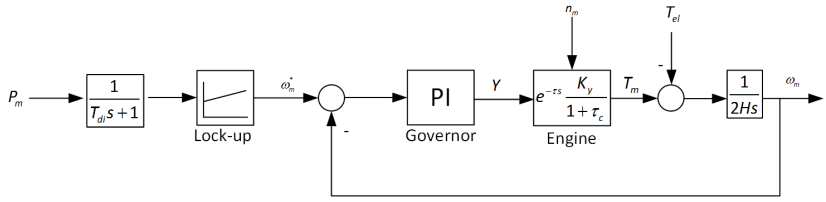

Figure 3.10: *Block diagram speed control loop including lockup-table for optimal speed reference.*

A simulation of the diesel engine is performed with step-changes in the load torque according to the test bench in figure 3.3. of $\frac{1}{3}\,pu$. Minimum speed reference was set to $n_m = 0.5\,pu$ Due to the limitations of maximum output torque, the applied load torque must be a factor lower than $T_{m,max}$ in order to accelerate the engine speed. An appropriate factor was found to be 0.97. Maximal allowable load torque will then be given as

$$T_l \leq 0.97 T_{m,max} \tag{3.40}$$

This limitation of the load torque is adequate to state since it will be possible to control the output electrical power of the generator through the voltage-exciter controller. Figure 3.11 shows the load torque applied in the simulation with limitation according to equation 3.40. Figure 3.12 shows the corresponding speed response. When the load torque drops to zero, the engine speed is only slowly decelerating due to inertia in the drive train.

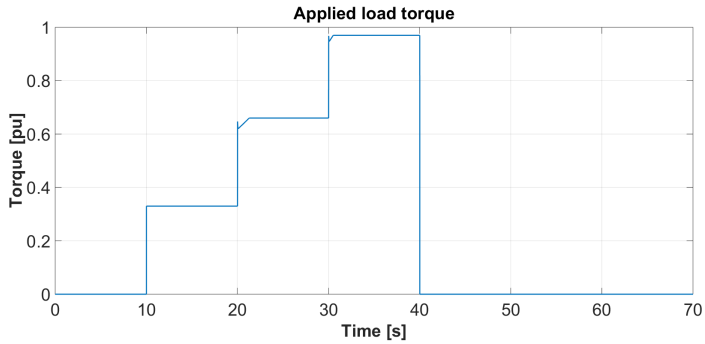

Figure 3.11: *Load torque applied for isolated test of speed engine. The load torque is limited by maximal allowable load torque according to equation 3.40, and hence cut edges can be seen*

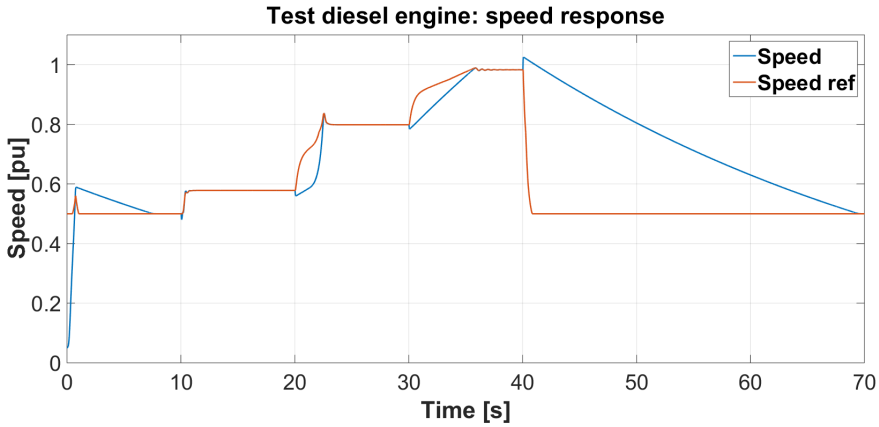

Figure 3.12: *Resulting speed response from load torque applied in figure 3.12. The red line is the reference speed yielding optimal fuel consumption. The blue line the actual engine speed.*

3.3.5 Estimation of fuel consumption

In order to evaluate fuel consumption of diesel engines, an approximations of SFOC [gr/kWh] with respect to different speed levels has been carried out. According to [45] the hourly fuel consumption of an internal combustion engine for a given fixed speed can be approximated by a quadratic function of the load expressed in equation 3.41 .

$$C_1 = C_0 + aP_m + bP_m^2 \tag{3.41}$$

Expressing C_1 in $[gr/h]$, SFOC is obtained by

$$SFOC = \frac{C_1}{P_m} = \frac{C_0}{P_m} + a + bP_m \tag{3.42}$$

In this thesis, SFOC is approximated for the five selected speed levels $\omega_m = 0.6$, 0.7, 0.8, 0.9 and 1, *pu* by using quadratic regression in Microsoft Excel. The SFOC for an arbitrary speed level is estimated by using linear interpolation between the SFOC-approximations. The support points for the SFOC-approximations have been taken from readings in figure 2.2. The Matlab-script for estimation of SFOC is given in appendix section A.4. In figure 3.13, the approximated SFOC-curve for $\omega_m = 1\,pu$ and the corresponding support points, are plotted against engine load. Approximations for all the five selected speed levels are shown in figure 3.14.

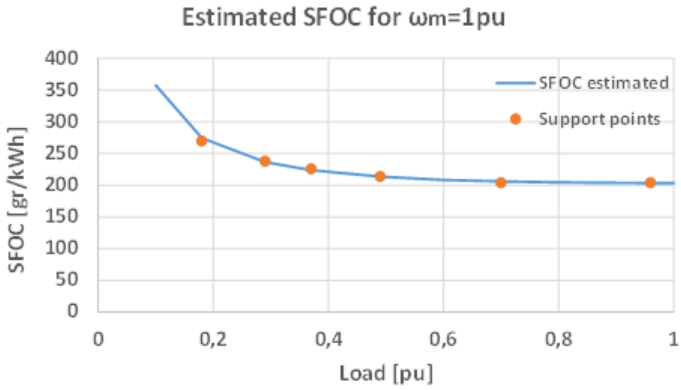

Figure 3.13: *The figure shows the estimated SFOC-curve for $\omega_m = 1\,pu$. The red points are the corresponding support points.*

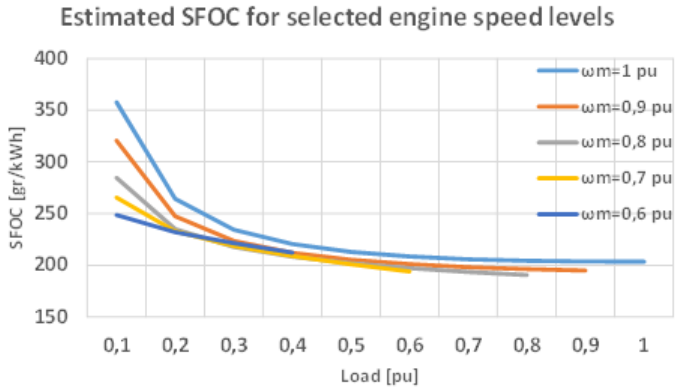

Figure 3.14: *Estimation of SFOC using quadratic regression for selected speed levels. Interpolation is performed for obtaining SFOC for speed levels between the estimated curves.*

3.4 Battery storage system

The battery storage system composes of a battery bank and a bidirectional converter. A model of a Li-ion battery is provided from the Simulink library (figure 3.15). Experimental testing of this battery model has shown an accuracy of the dynamic behavior within an error ±5% for SOC between 20% and 100% [46]. Expression for battery voltage in discharge and charge mode are given by equation 3.43 and 3.44. The term i^*, is the battery current filtered through a low-pass current. For high load currents, i^* will cause a reduction of the battery-voltage which gives increased conduction losses. The battery resistance R_{Bat}, is internally calculated by the Simulink-model to $R_{bat} = 1\,m\Omega$.

$$E_{discharge} = E_0^{batt} - K\frac{Q_{tot}}{Q_{tot} - SOC} \cdot (it + i^*) + Ae^{-B \cdot it}, \quad i^* > 0 \tag{3.43}$$

$$E_{charge} = E_0^{batt} - K\frac{Q_{tot}}{SOC - 0.1 \cdot Q_{tot}} \cdot i^* - K\frac{Q_{tot}}{Q_{tot} - SOC} \cdot SOC + Ae^{-B \cdot SOC}, \quad i^* < 0 \tag{3.44}$$

The battery bank is composing of Li-NMC batteries connected together in series and parallel in order to supply or absorb a power of $800\,kW$ in the whole voltage range. Data-sheet for one battery module is provided from Corvus Energy [47]. The battery resistance is internally calculated by the Simulink-model to $R_{bat} = 1\,m\Omega$. Specifications of the battery bank is summarized in table 3.3

				Discharge		Charge	
Modules in series	Modules in parallel	Capacity [Ah]	Voltage min-max [V]	Current peak [A]	Current continuous [A]	Current peak [A]	Current continuous [A]
1	1	75	77-101	750	450	375	225
5	10	3750	385-505	7550	4500	3750	2250

Table 3.3: *Specifications of battery bank. Battery resistance is internally calculated by the Simulink-model to $R_{bat} = 1\,m\Omega$ Data-sheet for one battery module is provided from Corvus Energy [47]*

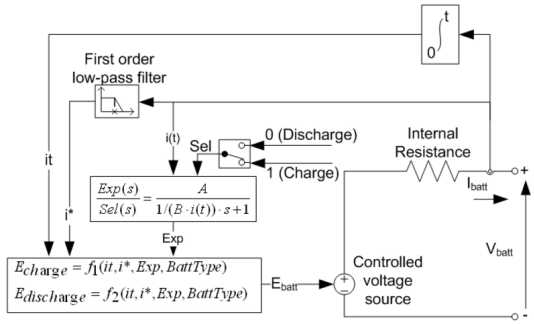

Figure 3.15: *Battery model provided from Simulink library. Source: [48]*

3.4.1 Bidirectional converter

Topologies of bidirectional converters can be classified into non-isolated and isolated converters. In the isolated converters the voltage-sides are galvanic isolated, i.e. by transformers. In many applications, is galvanically isolation is required due to correct operation of protection system and personnel safety [49]. When the voltage ratio between the converter sides becomes large, the non-isolated converters will be impractical. However, the non-isolated types have simple structure, cheaper and lower losses [49].

In this thesis a non-isolated converter has been implemented. The conceptual topology of this converter is shown in figure 3.16. The converter operates as a boost converter when current flows into the DC-link and buck converter when current is flowing into the battery. Depending on buck or boost mode, only one of the switches will be activated at a time. The switches are of the type insulated gate bipolar transistor (IGBT). The control signal d to the IGBTs are generated from a PWM-generator provided in the Simulink library [50].

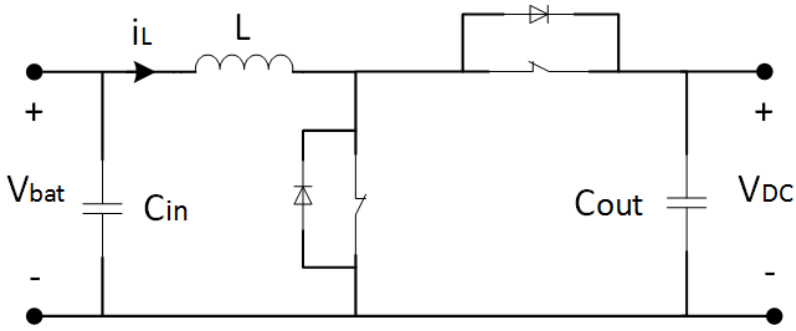

Figure 3.16: *Topology of the bidirectional converter connecting the battery to the DC-link.*

3.4.2 Selection of converter parameters

The battery bank comprises a costly unit in a hybrid power system. Switching frequency, filter capacitors and inductor should be chosen in order to mitigate battery aging. Heat development is a major factor of battery aging and an increase of internal losses in the battery results in additional heat development. In [51] is it shown that battery impedance increases with higher switching frequency ($5 - 20kHz$) due to skin and proximity effects. The severity of ripple current at high frequency switching may however be discussed. In [52], ripple effects on the battery aging are experimentally tested. According to the results in this study, cannot the battery aging be linked to current ripple. The same study shows, however, that current ripples have significant impact on the battery management system as maximum cell voltage over the individual battery cells may be exceeded. Electrical companies tend to recommend small ripples in voltage and current for prolonged life time. According to [53] is $\Delta i = 5\,\%$ of rated ampere-hour capacity and $\Delta V_{Bat} = 0.5\,\%$

suggested.

Concerning switching frequency of IGBTs, low switching frequency is desired for reduced converter losses. This is due to that AC-losses reduce and the fact that switching losses are proportional with the switching frequency [54]. However, low switching frequency is on expense of the dynamic response of converter controllers. Based on performance and the discussion above, converter parameters are selected as shown in 3.4. Sizes of L and C_{in} are calculated according to equation 3.45 and 3.46 [36, p. 170]. Output capacitor is the same as the smoothing capacitor of the diode bridge.

$$L = \frac{V_{Bat}(1-D)}{f_s \Delta i_L} \tag{3.45}$$

$$C_{in} = \frac{\Delta i_L}{8 f s \Delta V_{bat}} \tag{3.46}$$

f_s	$3000\,Hz$
C_{in}	$0.42\,mF$
ΔV_{bat}	$20\,V$
C_{out}[1]	$15\,mF$
L	$0.38\,mH$
Δi_L	$200\,A$ (at $V_{bat} = 400\,V$)
R_{on}	$1m\Omega$

Table 3.4: *Paramaters and specifications battery converter*

3.4.3 Converter controller

The converter controller composes of a cascaded controller with an outer and inner control loop. The outer-loop controls the output voltage of the converter i.e. the DC-link voltage V_{DC}. The inner loop controls the inductor current i_L by giving a reference to the duty ratio d. The inner-loop receives its current reference i_L^* from the outer-loop. Block diagram of control-structure is shown in figure 3.18. In order to design control parameters, the system-behavior of the converter is investigated through an equivalent circuit shown in 3.17. In this equivalent circuit, the switches are replaced by the average switching states and in addition is the inductor resistance R_L and the load R_{CPL} also included [55].

1. C_{out} equals the smoothing capacitor C in the DC-link. Only for design of controllers C_{out} is $15mF$. Else in the thesis it is set to $20\,mF$

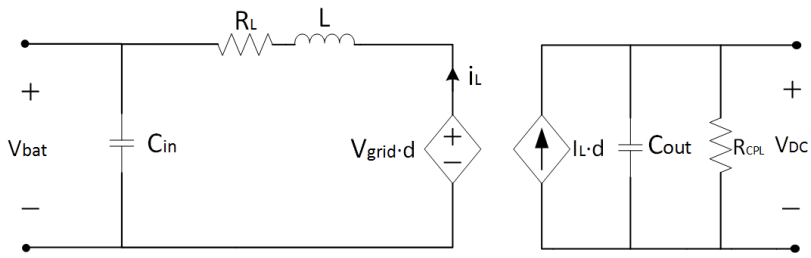

Figure 3.17: *Equivalent circuit for the bidirectional converter*

From figure 3.17, equation 3.47 and 3.48 can be framed by applying Kirchhoff's Voltage Law and Kirchhoff's Current Law respectively.

$$L\frac{di_L}{dt} = R_L i_L + V_{DC} \cdot d - V_{bat} \tag{3.47}$$

$$C_{out}\frac{dV_{DC}}{dt} = D \cdot i_L - \frac{V_{DC}}{R_{CPL}} \tag{3.48}$$

In equation 3.48, D denotes a stationary duty-ratio given by $D = \frac{V_{Bat}}{V_{DC}}$.

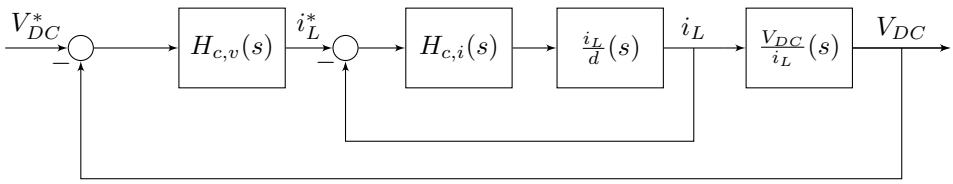

Figure 3.18: *Block diagram of the cascaded converter controller*

Current controller

By taking Laplace-transform of equation 3.47, an expression of the inductor current can be obtained

$$i_L = \frac{1}{R_L}\frac{V_{DC} \cdot d - V_{bat}}{L/R_L s + 1} \tag{3.49}$$

In equation 3.49 the duty ratio d represents the control signal from the current controller. Regarding control design for the system in equation 3.49, it will be possible to cancel out the term V_{bat} by adding a feed-forward coupling of the measured battery voltage and DC-link voltage. The feed-forward couplings have an advantage since the controller will be adapted to battery voltage variations according to its SOC. The expression of d with the feed-forward added, can be written as

$$d = \frac{H_c(s)e}{V_{DC}} + \frac{V_{bat}}{V_{DC}} \tag{3.50}$$

where $H_{c,i}(s)$ denotes the transfer function of the current controller and e the measurement error. Inserting equation 3.50 for d in equation 3.49 results in

$$i_L = \frac{1}{R_L} \frac{\not{V}_{DC}(\frac{H_{c,i}(s)e}{\not{V}_{DC}} + \frac{V_{bat}}{\not{V}_{DC}}) - V_{bat}}{\frac{LS}{R_L} + 1}$$

$$\Rightarrow i_L = \frac{1}{R_L} \frac{H_{c,i}(s)e}{\frac{L}{R_L}s + 1} \tag{3.51}$$

Due to the switching in the PWM, d will have a delay which can be represented by a first-order time delay given in equation 3.52.

$$H_{sw}(s) = \frac{1}{T_{sw}s + 1}d \tag{3.52}$$

The switching time delay T_{sw} can be equated to a half of the switching period. i.e $T_{sw} = \frac{1}{2f_s}$ [56, p. 94]. The complete block diagram of the current control loop including controller with feed-forward, the time delay in equation 3.52 and a measurement time delay is shown in figure 3.19.

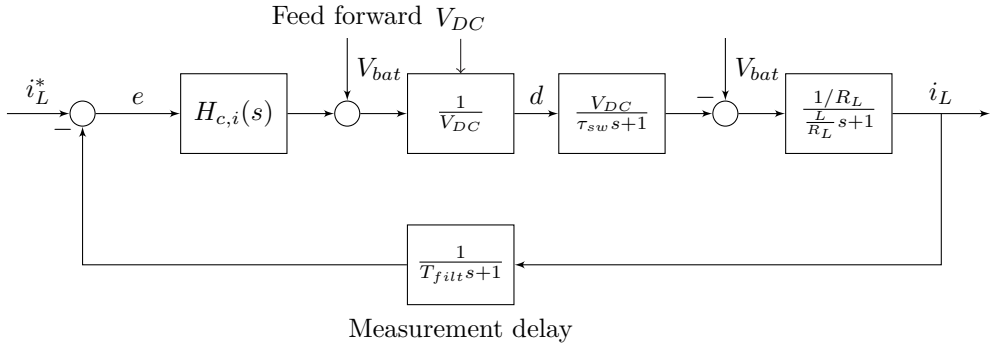

Figure 3.19: *Block diagram of the current control loop*

As the feed-forward coupling cancels out the term V_{bat}, the resulting system, for which the controller $H_c(s)$ is to be designed, will comprise two first-order transfer function. For this control design a PI-controller will be suitable. The equivalent control loop for design of the PI-controller is shown in figure 3.20.

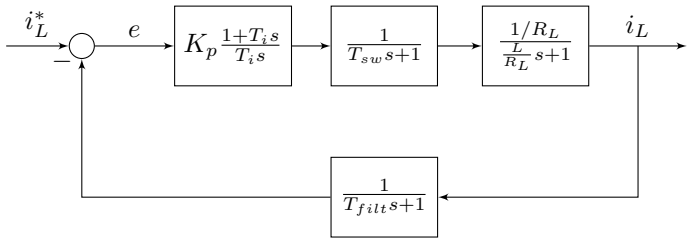

Figure 3.20: *Resulting control loop when disturbances from V_{bat} has been eliminated by feed-forward couplings.*

The control parameter of the PI-controller can be designed by using modulus optimum, where the dominant time constant $\frac{L}{R_L}$ will be canceled out. With modulus optimum, control parameters can be obtained based on equation 3.53 and 3.54 (see appendix section A.5). The value of K_{pi} in equation 3.54 is multiplied by three for higher bandwidth.

$$T_{ii} = \frac{L}{R_L} \tag{3.53}$$

$$K_{pi} = \frac{T_i}{2\frac{1}{R_L}T_{sum}}, \quad T_{sum} = T_{sw} + T_{filt} \tag{3.54}$$

$T_{ii} = 0.38$	$K_{pi} = 0.3$	$T_{sw} = 0.33ms$	$T_{filt} = 1.67ms$

Table 3.5: *Control parameters of speed controller. K_{pi} is multiplied by three compared to the modulus optimum criteria*

Since the value of $K_{p,i}$ is multiplied by three, compared to the modulus optimum criteria, the closed loop of a modulus optimum design will result in a time constant of $\frac{2T_{sum}}{3}$. This time constant will be considered for modeling the outer control-loop. Figure 3.21 shows open and closed loop bode-diagram of the current controller.

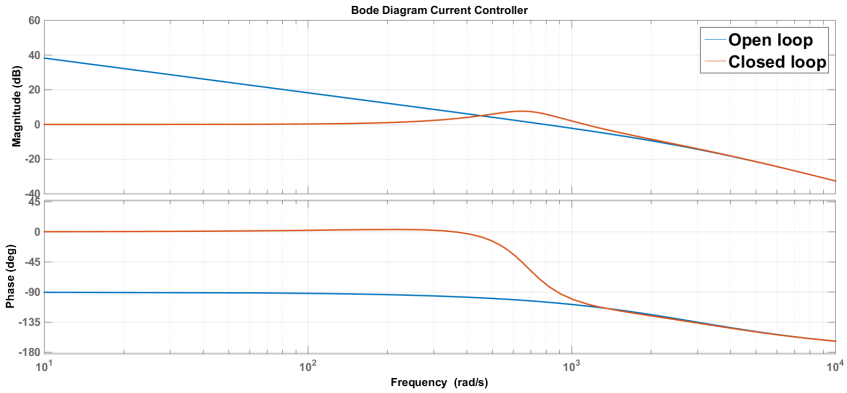

Figure 3.21: *Bode diagram of open and closed loop of the current controller. Bandwidth* $= 780\,rad/s$, $PM = 75.4°$

Voltage controller

To model the voltage controller, the closed loop of the current controller and the physical system from inductor current to the DC-link voltage must be considered. The closed loop of the inner control loop can be equated by a first order transfer function with equivalent time coefficient $\frac{2T_{sum}}{3}$ from the current control loop [57]. By taking Laplace transform of equation 3.48, equation 3.55 can be framed. This equation expresses the relationship from the inductor current to output voltage. The resulting block diagram of the outer loop can be established as shown in figure 3.22.

$$V_{DC} = \frac{D}{C_{out}R_{CPL}s + \frac{1}{R_{CPL}}}I_L \tag{3.55}$$

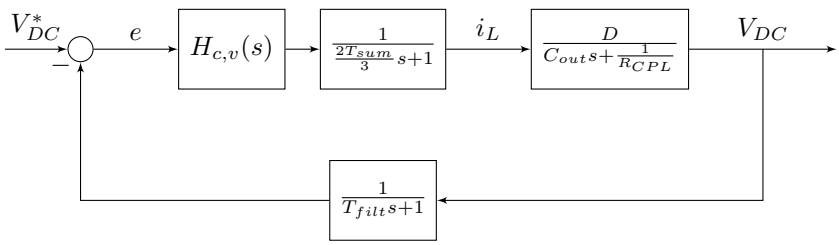

Figure 3.22: *Control loop of voltage controller*

Regarding design of the voltage controller, the no-load situation is considered. At no-load, when R_{CPL} is set infinity, equation 3.55 becomes an integral-term as shown in equation 3.56. Control-parameters will therefore be tuned based on symmetrical optimum when using a PI-controller.

$$V_{DC} = \frac{D}{C_{out}s} I_L \tag{3.56}$$

By using symmetrical optimum, control parameters of $H_{C,v}(s)$, are selected according to equation 3.57 and 3.58. Table 3.6 summarizes control parameters.

$$T_{i,v} = \beta T_{eq}, \quad \beta = 4, \quad T_{eq} = \frac{2T_{sum}}{3} + T_{filt} \tag{3.57}$$

$$K_{p,v} = \frac{C_{out}}{\sqrt{\beta} D T_{eq}} \tag{3.58}$$

$T_{io} = 0.018$	$K_{po} = 3.83$	$T_{sum} = 1.8ms$	$T_{filt} = 3.3ms$

Table 3.6: *Control parameters of voltage controller*

Figure 3.23 shows the bode diagram of the voltage controller at no load. The bode diagram for the voltage controller at full load is shown in figure 3.24. Due to the negative sign of R_{CPL}, the phase will initially start at $-270°$ and cross $-180°$ when the magnitude has a positive gain. However, acceptable tracking can still be obtained as long as the magnitude is large enough when the phase is $-180°$.

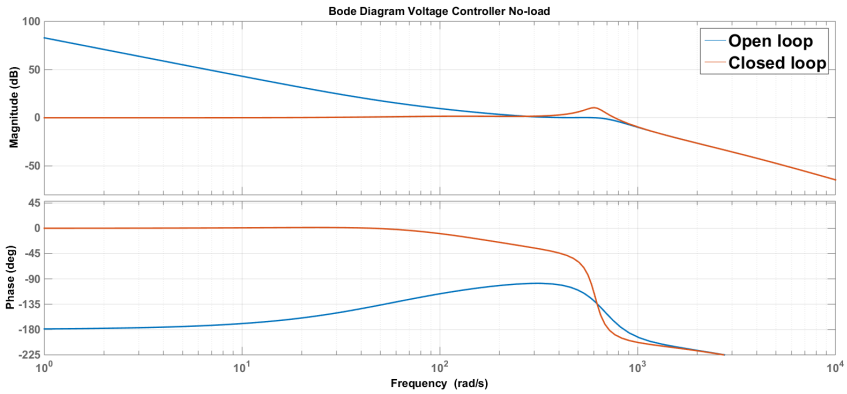

Figure 3.23: *Bode diagram of open and closed loop at no load of the voltage controller. Bandwidth* $= 254\,rad/s$. $PM = 61°$

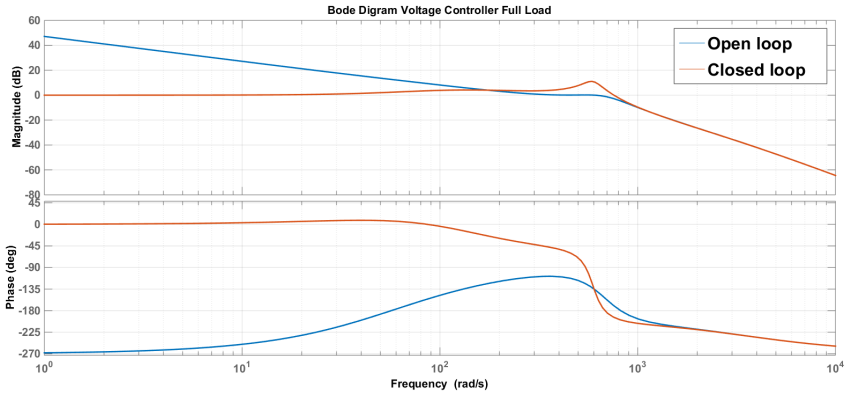

Figure 3.24: *Bode diagram of open and closed loop at full load of the voltage controller. Full load is calculated by* $R_{CPL} = \frac{(930\,V)^2}{800\,kW}$. *Bandwidth* $= 240\,rad/s$, $PM = 46°$

3.4.4 Testing of converter controller

A test of the converter controllers is performed according to the test bench of figure 3.3. The load is set both positive and negative in order to validate performance of the converter controller in both buck and boost mode. Figure 3.25 shows resulting inductor current from this simulation. Spikes in the current occurring at load changes are far from reaching maximum battery current levels according to table 3.3. Current ripples are around $200\,A$, which also is the size of the ripple the inductor is dimensioned to yield.

The response of the DC-link voltage in figure 3.26, shows large voltage dips when the load increases after $6\,s$. However, thruster systems may be equipped with low voltage protection which prevents power to be drown under a certain voltage limit. When the load drops drop from full load to zero load, the voltage reaches beyond $1150\,V$. To reduce this over-voltage, bandwidths of the control loops might be attempted to be even more increased. Otherwise would increasing switching frequency and a larger DC-link capacitor be effective measures.

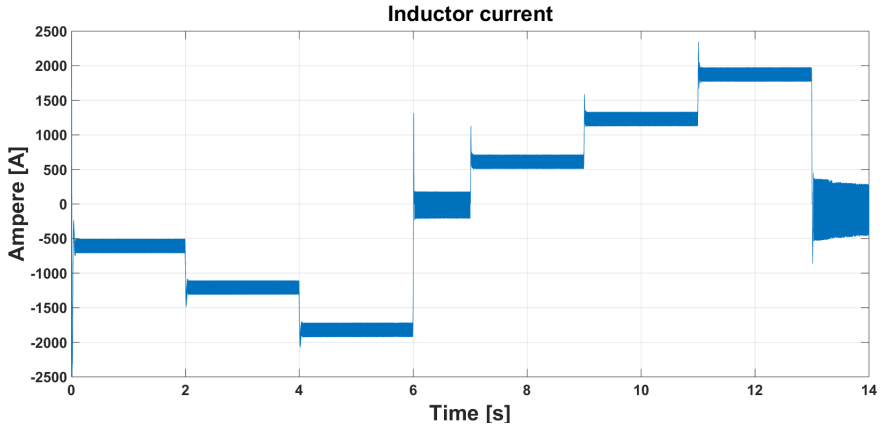

Figure 3.25: *Performance test converter controller: Inductor current*

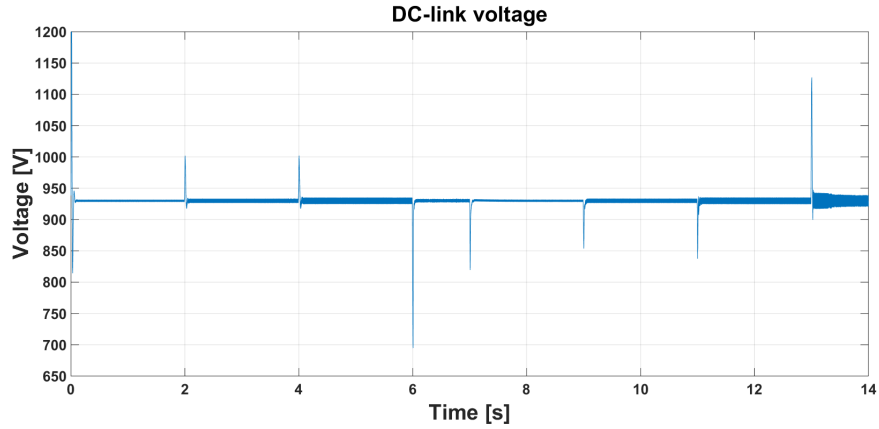

Figure 3.26: *Performance test converter controller: DC-link voltage*

4 | Control structures of diesel generators and battery

First in this chapter, the performance of diesel generators operating alone is investigated. For this purpose, two different exciter-voltage controllers for control of DC-link voltage are designed. Next, the battery will be added to the power system. Two different control configurations for power share between the battery and generator sets are investigated in this regard. All the control structures, are simulated and tested with the bench-test explained in section 3.1.3. Simulations of power-waveforms with values expressed in per-unit, are with respect to the nominal value of the synchronous generator i.e. $800\,kW$. Power waveforms of battery and generators are also filtered through a low-pass filter.

4.1 Diesel generator sets operating alone

4.1.1 System equations

The physical system that will be investigated regarding design of exciter-voltage controllers, are the control loop from the input of the exciter machine to the DC-link voltage. The transfer function from the exciter machine to terminal voltage is shown again in equation 4.2. From the equivalent circuit in figure 3.5, the transfer function from the voltage at the terminals of the generator to the DC-link voltage can be expressed according to equation 4.1. Derivation is given in appendix section B.1.

$$\frac{V_{DC}}{V_t}(s) = \frac{3\sqrt{2}}{\pi} \frac{\frac{R_{CPL}}{R_{CPL}+R_k}}{s^2 \frac{R_{CPL}CL_k}{R_{CPL}+R_k} + s\frac{CR_kR_{CPL}+L_k}{R_{CPL}+R_k} + 1} \tag{4.1}$$

$$\frac{v_t}{v_f^*}(s) = \frac{1}{\tau_{ex}s+1} \cdot \frac{1}{1+T'_{d0}} \tag{4.2}$$

In equation 4.1, R_{CPL} is inserted with a negative sign. According to the first criterion of Routh's Criteria, the system will be unstable i.e. has positive poles, if one of the polynomial time coefficients in the denominator are negative [44, p. 260]. In order to have positive time coefficients, the following inequalities can be identified

$$R_{CPL} > R_k \tag{4.3}$$

$$CR_kR_{CPL} > L_k \tag{4.4}$$

These inequalities show that the size of capacitor cannot be too small. Reduction of R_{CPL} also may cause instability. Low voltage and high load are factors that reduces

R_{CPL}. In order to frame the complete stability criteria of the voltage control loop, Routh's table can be applied to the closed loop system. In the design of voltage controllers, the R_{CPL} corresponding to full load will be applied, which yields the lowest R_{CPL}. The time coefficient in equation 4.1, which are labeled t_1 and t_2 are calculated based on the per-unit base-values of the synchronous machine. The field voltage output from the exciter voltage-controller is limited by $v_{f,max}$ and $v_{f,min}$. Table 4.1 summarizes parameters of the control loop.

$t_1 = \frac{R_{CPL}CL_k}{R_{CPL}+R_k} = 11.5\mu s^2$	$t_2 = \frac{CR_kR_{CPL}+L_k}{R_{CPL}+R_k} = 2.91ms$	$\frac{R_{CPL}}{R_{CPL}+R_k} = 1.15$	$T'_{d0} = 7.55\,s$
$\tau_{ex} = 0.19\,s$	$v_{f,max} = 4.5\,pu$	$v_{f,min} = -4.5\,pu$	

Table 4.1: *Specifications of the control loop investigated to design voltage controllers. R_{CPL} is considered at full load yielding $\frac{(930\,V)^2}{(800\,kW)}$. Commutation inductance is considered $L_k = L''_d$.*

4.1.2 Droop control

To control the DC-link voltage and subsequently split the power demand between the two generators, droop control has been implemented. This is a widely used method that does not require communication between the generators [5]. In principle by using the droop control method, one generator supplies a higher amount of power than the other one. If the generators were supplying the same amount of power, the system would be unstable as generators would fight each other in order to control the load. The implementation of the droop control is realized through a linear voltage drop in the reference voltage according to the power the generator supplies. Despite the drooping characteristic, constant voltage DC-link voltage can still be obtained by feeding a compensating voltage reference from a secondary control level [58]. Equation 4.5 shows the characteristic equation for the droop controller. V_0 is the voltage reference at no load and δ is the slope which defines at which rate the voltage drops.

$$V^*_{DC} = V_0 - \delta P_{gen} \tag{4.5}$$

Values of δ and V_0 can be obtained according to equation 4.6 and 4.7 [58].

$$\delta = \frac{\Delta V_{max}}{P_{max}} \tag{4.6}$$

$$V_0 = V_{DC,n} + \frac{\Delta V_{max}}{2} \tag{4.7}$$

In figure 4.1, the droop characteristic of two generators sharing load is depicted. At a given load situation causing a voltage of $1\,pu$, the share of power between the generators will be 0.4 and $0.6\,pu$.

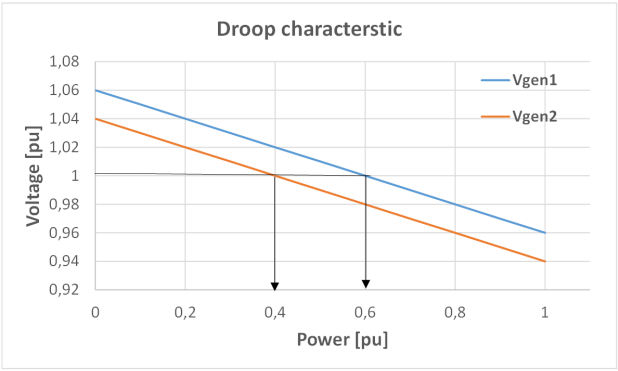

Figure 4.1: *Droop characteristic of two generators sharing load*

The actual share of power between the generators for a total demand of P_{tot} can be calculated by equation 4.8 and 4.9. See derivation in appendix section B.2. The generator with the highest reference voltage, will also supply the highest amount of power.

$$P_{gen2} = \frac{V_{02} - V_{01} + P_{tot}\delta_1}{\delta_1 + \delta_2} \tag{4.8}$$

$$P_{gen1} = P_{tot} - P_{gen2} \tag{4.9}$$

If δ_1 and δ_2 are equal, the power difference $P_{gen1} - P_{gen2}$ will always be equal. The power difference then becomes

$$P_{gen2} - P_{gen1} = \frac{V_{02} - V_{01}}{2\delta} \tag{4.10}$$

4.1.3 Interactions between diesel engine and generator

The diesel engine and the synchronous generator composes a power train on the same shaft, at which the generator exerts a load torque on the diesel engine. The power-delivering process starts with the exciter-voltage controller which takes action based on the grid load that affects the DC-link voltage. Adjusting the field voltage controller causes an electromagnetic torque that must be responded by the output torque i.e. fuel injection of the diesel engine in order to keep its reference speed. For a given speed, power is directly proportional to torque. The transfer of power from the diesel engine to generator can be expressed as follows

$$P_m = \omega_m \cdot T_m = P_{gen} \tag{4.11}$$

To obtain stable operation, it will be important that the voltage control loop is sufficient faster operating than the speed control-loop of the diesel engine. Otherwise, sudden speed changes would result in disturbances in the DC-link voltage. The band-width of the speed loop can be effectively reduced by increasing the time constant T_{di} mentioned in section 3.3.4. Experimentations with the value of T_{di}, has shown that it should be

increased more than what would yield a decade behind the band-with of the field voltage controller. Increasing T_{di}, however, slows the dynamic response of the diesel engine. Figure 4.2 shows the DC-link voltage from simulations with different T_{di} under steady load conditions. It can be seen that lowering T_{di} from 5 to 2.5 seconds causes instability. In figure 4.3, the corresponding speed of generator sets to the simulation of $T_{di} = 2.5\,s$ is depicted. As can be seen, the speeds are never reaching a steady value.

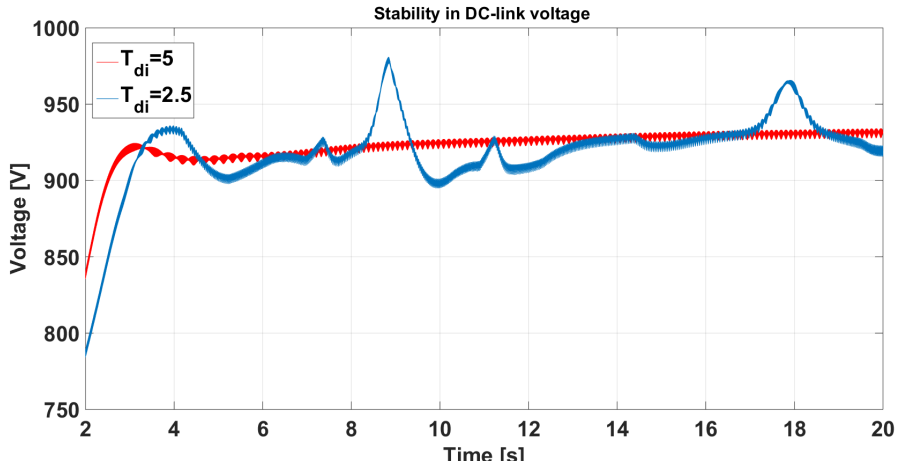

Figure 4.2: *Resulting DC-link voltage with two different values of T_{di} in diesel engines. Simulations were performed with a steady load at 1 pu. Voltage controller was as modeled in section 4.1.4*

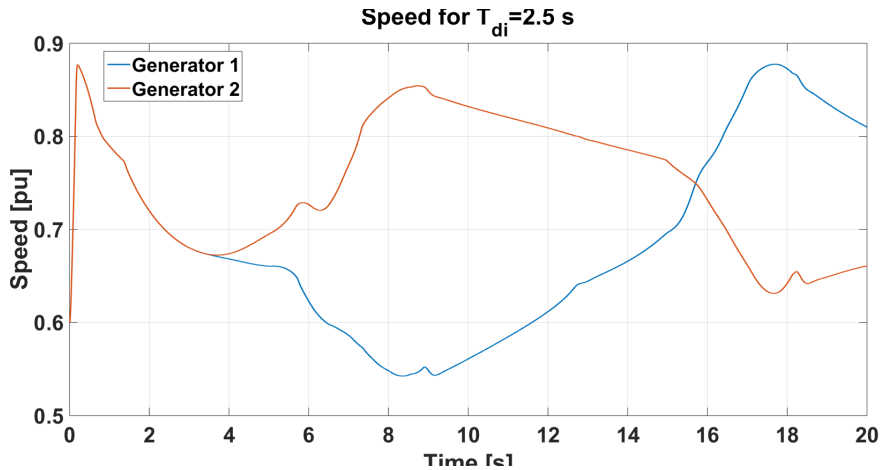

Figure 4.3: *Engine speeds of generator sets with $T_{di} = 2.5\,s$*

4.1.4 Single voltage-controller

In this control structure, DC-link voltage is controlled directly by one controller for each generator. The control structure is shown in figure 4.4.

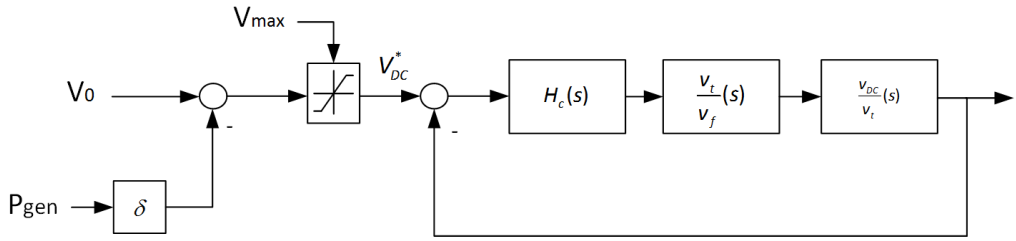

Figure 4.4: *Block diagram of droop control with a single voltage controller.*

The structure uses droop control to feed the reference voltage V^*_{DC}. The drooping slope δ is set equal for both generators which gives the power share according to equation 4.10. The maximum allowable voltage reference V_{max} is in correspondence with the maximum output torque of the diesel engine mentioned in section 3.3.4. Expressing equation 4.11 in terms of voltage and current and including mechanical losses, the following inequality can be framed

$$\omega_m \cdot T_{m,max} - \omega_m C_r > P_{gen} > V_{max} I_{dc} \tag{4.12}$$

which results in the maximal allowable voltage reference

$$\Rightarrow V_{max} < \frac{\omega_m (T_{m,max} - C_r)}{I_{dc}} \tag{4.13}$$

Considering a PI-controller for this control loop, modulus optimum can be applied where the T_i term cancels out T'_{d0}. The time constants t_1 and t_2 in equation 4.1 can be added in T_{sum} together with τ_{ex}. However, the time constants in $\frac{v_{DC}}{v_t}(s)$ are negligible small compared to τ_{ex}. Since the output voltage has very low ripple, the filtering coefficient T_{filt} can also be set very small. The control parameters were set according to table 4.2. Bode diagram of open and closed loop for full load is shown in figure 4.5.The closed loop indicates good tracking and small overshoot. The bandwidth of the open loop is as low as $4\,rad/s$, which will demand a higher T_{di} of the diesel engine.

$K_p = 40$	$T_i = 7.55$	$V_{01} = 1.05\,pu$	$V_{02} = 1.06\,pu$	$\delta = 0.1$	$T_{di,c} = 6\,s$	$T_{filt} = 0.5\,ms$

Table 4.2: *Control parameter of the single voltage-controller.*

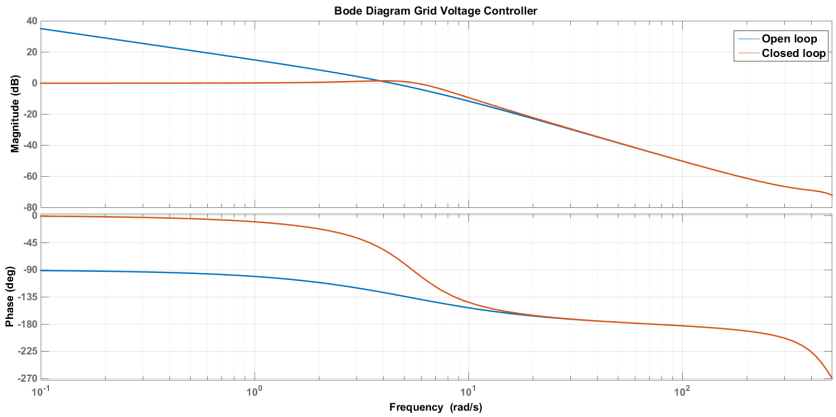

Figure 4.5: *Bode diagram of single voltage-control loop. Bandwidth* $= 4.04\,rad/s$. $PM = 52°$

4.1.5 Performance test single voltage control

In the performance test of the single voltage-controller, the load was filtered through a low-pass filter with a time constant of $3\,s$. The output power of the generators, depicted in figure 4.6, can be seen to have oscillations in the load step at $20\,s$. The speed of the generator in figure 4.7, increases slowly as the power of generators increases. A slightly more sudden acceleration can be seen at $20.\,s$ Lowering T_{di} would cause the engine speed to accelerate more smoothly and also reduce the oscillations in output power. However, this would have limited the steepness of the load increments. The oscillations from the generators are also reflected in the DC-link voltage shown in figure 4.8. When the load is disconnected after $55\,s$, a large over-voltage raises from $885\,V$ and reaches $1288\,V$ and lasts for $1.6\,s$.

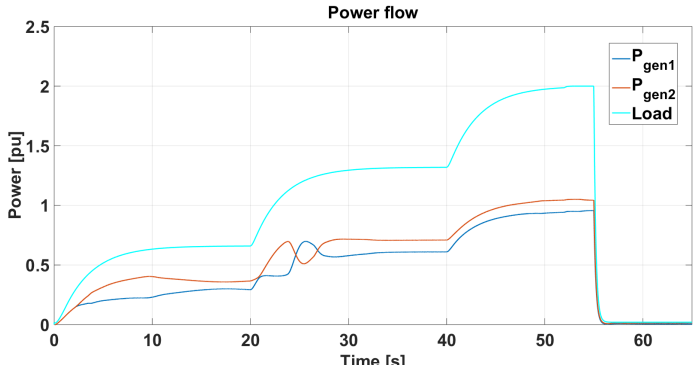

Figure 4.6: *Performance test of single voltage controller: power flow*

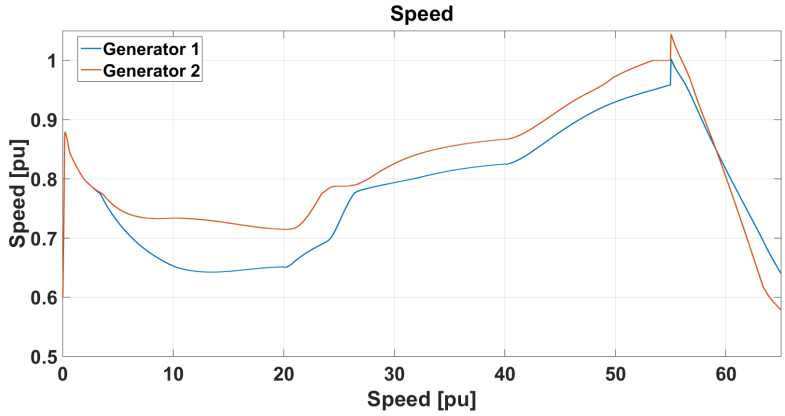

Figure 4.7: *Performance test single voltage controller: speed.*

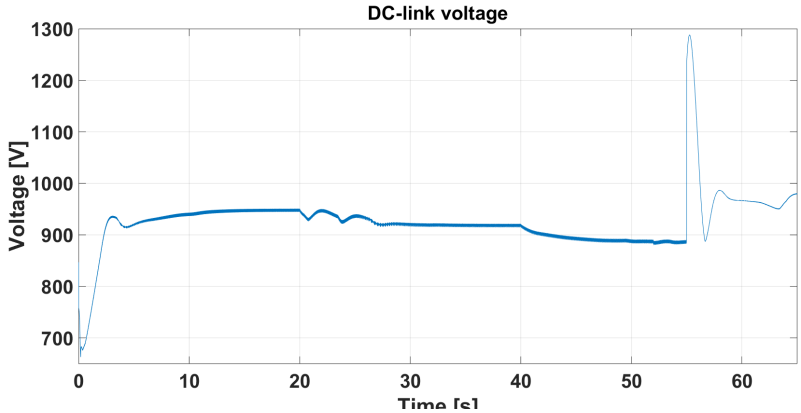

Figure 4.8: *Performance test single voltage controller: DC-link voltage. The over-voltage at* $55\,s$ *raises from* $885\,V$ *and reaches* $1288\,V$ *and lasts for* $1.6\,s$

4.1.6 Cascaded voltage controller

The second voltage controller that is tested is a cascaded controller where the inner-loop controls the AC-voltage at the terminal of the generator and the outer-loop the DC-link voltage. The reason for investigating this configuration is that the inner-loop controller is standard controller of a diesel generator. It might be that also controlling the terminal voltage, will yield faster and more stable operation of the generators. The block diagram of the cascaded control loop is shown in figure 4.9

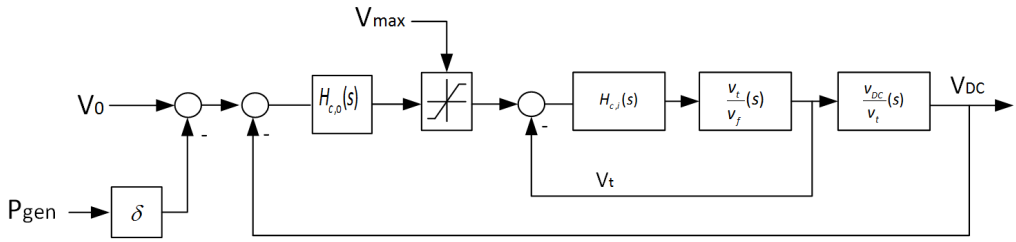

Figure 4.9: *Block diagram cascaded voltage controller*

According to the bode-diagram in figure 4.5, a PI-controller of the inner-loop will result in very low bandwidth of the outer-loop since this must be approximately one decade behind that of the inner-loop. To increase the bandwidth of the cascaded controller, and still have sufficient phase-margin, a PID-controller of the inner-loop is therefore proposed. The PID controller is on the form given in equation 4.14 and can be approximated to equation 4.15 if $T_i >> T_d$ and the filter coefficient $\alpha << T_d$ [44, p. 333].

$$H_{PID} = K_{pi}(1 + \frac{1}{T_{ii}s} + \frac{T_d s}{\alpha s + 1}) \tag{4.14}$$

$$H_{PID}(s) \approx K_{pi}\frac{(1 + T_{ii}s)(1 + T_d s)}{T_{ii}s(\alpha s + 1)} \tag{4.15}$$

By selecting $T_{ii} = T'_{d0}$ and $T_d = T_{ex}$, the open inner-loop can be written according to equation 4.16. K_{pi} can be selected to yield appropriate bandwidth.

$$H_{OL,i} = K_{pi}\frac{\cancel{(1 + T_i s)(1 + T_d s)}}{T_{ii}s(\alpha s + 1)} \cdot \frac{1}{\cancel{T_{ex}s + 1}} \cdot \frac{1}{\cancel{T'_{d0}s + 1}} = \frac{K_{pi}}{T_{ii}s(\alpha s + 1)} \tag{4.16}$$

The resulting control-loop for the outer-controller where a PI-controller will be used, then becomes

$$H_{CL,i}(s) = \frac{1}{s^2\frac{T_{ii}\alpha}{K_p} + s\frac{T_i}{K_p} + 1} \tag{4.17}$$

T_{eq} for the inner-loop is set to $T_{eq} = \frac{T_{ii}}{K_p}$. For the outer-loop PI-controller symmetrical optimum is used, with $T_{io} = 4T_{eq}$. K_{po} is adjusted to yield a bandwidth approximately one decade behind that of the inner-loop. Control parameter for the cascaded control

scheme is shown in table 4.3. Figure 4.10 shows the open loop bode diagram of the inner and outer-loop. Both of these control loops display good phase-margin. The bandwidth of the outer-loop is slightly lower than that of the single voltage-controller, which makes this control structure slightly slower. The corresponding closed loop bode diagram is shown in figure 4.11.

$K_{pi} = 200$	$T_{ii} = 7.55$	$T_d = 0.19$	$\alpha = 0.02$	$T_{io} = 0.15$	$K_{po} = 0.4$
$V_{01} = 1.05\,pu$	$V_{02} = 1.06\,pu$	$\delta = 0.1$	$T_{di} = 15$	$T_{filt} = 0.5\,ms$	

Table 4.3: *Parameter for the cascaded voltage control loop*

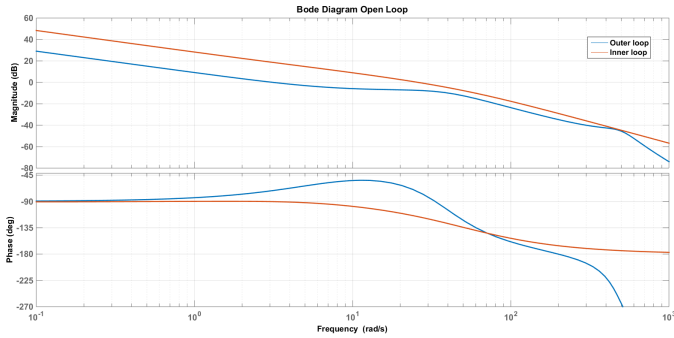

Figure 4.10: *Open loop bode diagram of both the inner and outer-loop of the cascaded voltage controller. Bandwidth inner and outer-loop:*$26\,rad/s$ *and* $3.2\,rad/s$*. PM inner and outer-loop:* $66°$ *and* $109°$

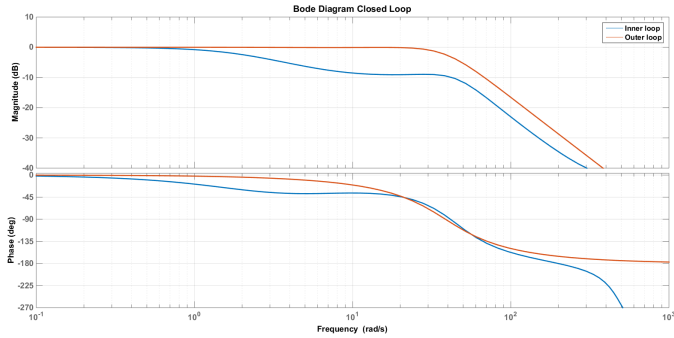

Figure 4.11: *Closed loop bode diagram of the cascaded voltage controller.*

4.1.7 Performance test cascaded voltage control loop

Simulations with the cascaded voltage controller shows that this control scheme fail to provide stability for a steady load. This results in oscillations of the output power of the generators as seen in figure 4.12 and in the speed in figure 4.13. The DC-link voltage in figure 4.14 reaches, however, a steady value after an overshoot. A simulation is also performed when speed is set fixed at $0.7\,pu$. The power flow from this simulation is shown in figure 4.15. Despite T_{di} initially is set as large as $15\,s$, the fixed speed operation considerable improve the stability, but small oscillations can still be seen.

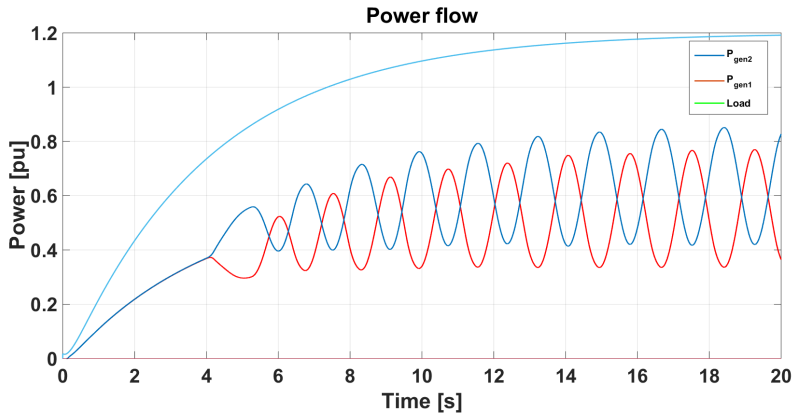

Figure 4.12: *Performance test cascaded voltage controller: power flow*

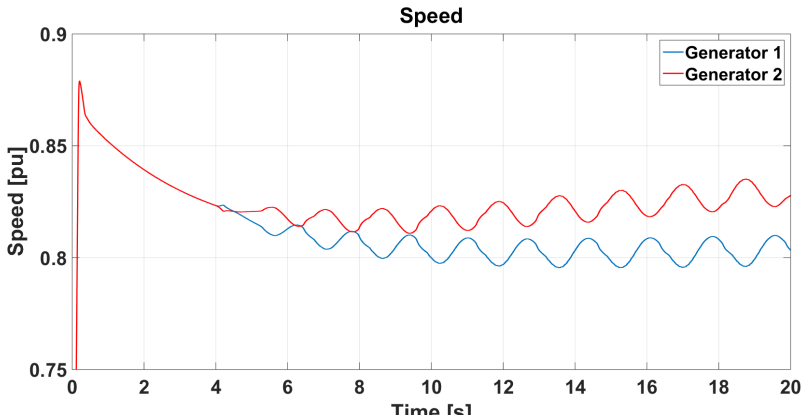

Figure 4.13: *Performance test cascaded voltage controller: speed*

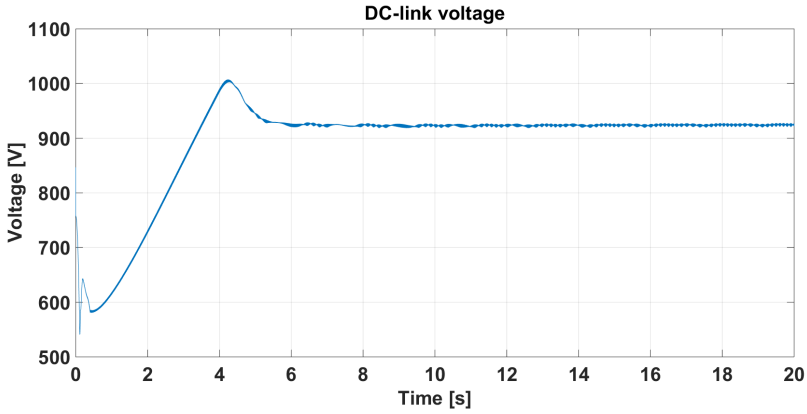

Figure 4.14: *Performance test cascaded voltage controller: DC-link voltage*

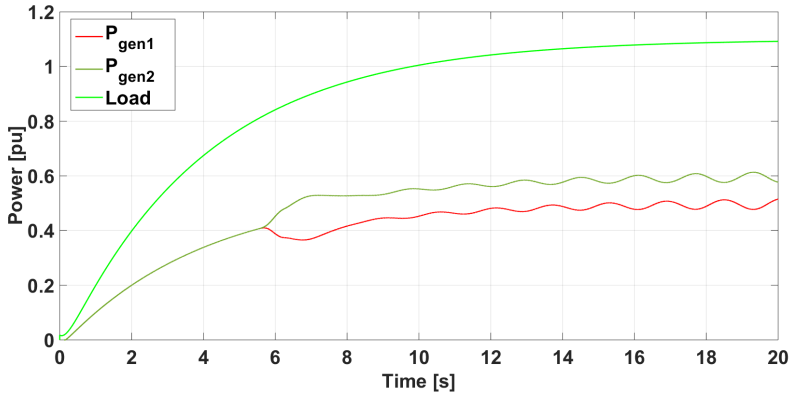

Figure 4.15: *Performance test cascaded voltage controller: power flow. In this simulation, speed has been set fixed at* $0.7\,pu$

4.1.8 Power controller for enhanced dynamic performance of diesel engine

According to stability findings in the sections above, T_{di} must be set sufficient large in order to obtain stability, which, however, slows down the dynamic response of the diesel generator. In this section a solution to improve the dynamic performance of the generator set is proposed. The idea of this solution is to control the deviation between the actual output power of the generator and an estimated output power P_{est}. The output of the controller is added to the speed reference of the diesel engine. The block diagram of the speed controller with this power controller added, is shown in figure 4.16.

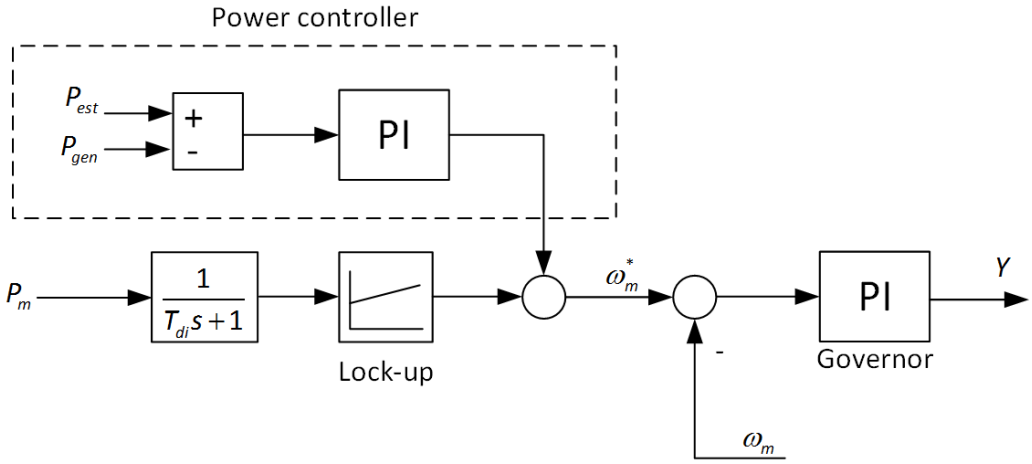

Figure 4.16: *Block diagram of the speed control loop with the power controller added.*

The estimated output power of each generator P_{est1} and P_{est2} is the output power which the generators are set to supply according their droop characteristic. For control od the DC-link voltage, the control structure and settings in section 4.1.4 are applied. As the drooping slope of the generators are equal and $V_{02} > V_{01}$, equation 4.10 can be applied to calculate P_{est1} and P_{est2} given in equation 4.18 and 4.19. This calculation requires also that the total load power P_{tot} is measured.

$$P_{est1} = P_{tot} - \frac{1}{2}\frac{V_{02} - V_{01}}{2\delta} \tag{4.18}$$

$$P_{est2} = P_{tot} + \frac{1}{2}\frac{V_{02} - V_{01}}{2\delta} \tag{4.19}$$

Regarding the design of the power controller, which is a PI-controller, the integral time constant of the governor must be considered. The integral time coefficient $T_{i,p}$ of the power controller, is found to appropriate when $T_{i,p}$ is at least the double of that of single-voltage controller. This causes the integral effect to end at $\frac{1}{T_{ip}}$. The control gain, K_{pp} is set unity.

A possible drawback of adding the power controller is that it may cause more acceleration of the diesel engine and distort optimal speed reference, which is bad for the fuel consumption. To reduce the contribution of the power controller, T_{ip} can be increased. Control parameters with the power controller applied, have been set according to table 4.4. The structure and parameters of the voltage exciter controller are the same as in section 4.1.4.

$T_{di} = 2.5\,pu$	$T_{i,p} = 20$	$K_{p,p} = 1$

Table 4.4: *Control parameters for when power control of diesel engine is added. Other parameters are the same as in section 4.1.4.*

4.1.9 Performance test with power control of diesel engine

With power controller added in the diesel engine, the load is allowed to increase faster than in section 4.1.4. Smoothing filter coefficient of the load is in this case set to $1.5\,s$. The power flow depicted in figure 4.17 also shows more even operation of the generator sets. The output of the power controllers which are added to the speed reference, is shown in figure 4.19. This contribution is never above $\pm 0.02\,pu$ and approaches zero when the load increases. The engine speeds, depicted in figure 4.18, can be seen to have an even acceleration. The voltage peak that arises when the load drops, raises from $885\,V$ to $1280.5\,V$ and lasts approximately for $1.6\,s$. The reason for this slightly lower voltage peak than in section 4.1.4, may be that the power controllers immediately lower the speed reference of the diesel engine when the load change occurs.

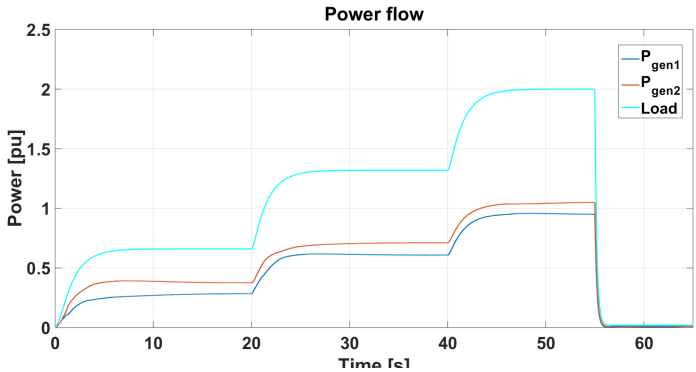

Figure 4.17: *Power flow with power controller added to the diesel engine.*

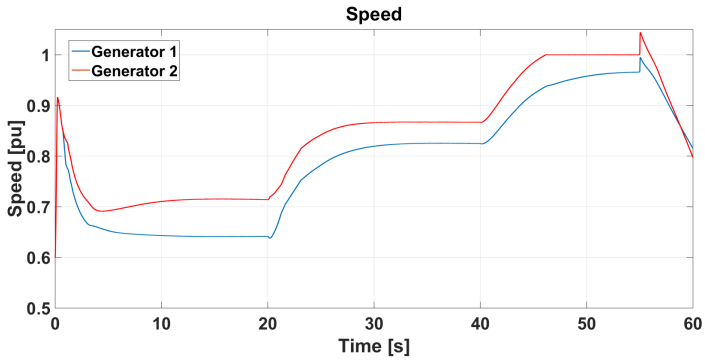

Figure 4.18: *Engine speed with power controller added to the diesel engine*

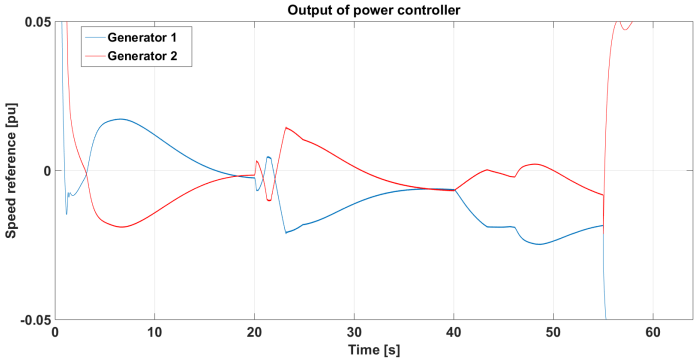

Figure 4.19: *Output from power controller. The vertical axis shows speed since the output of the power controller gives a contribution to the speed reference of the diesel engine.*

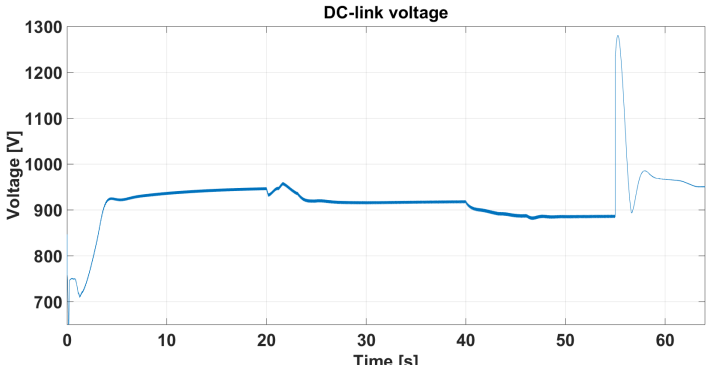

Figure 4.20: *Grid voltage with power controller added to the diesel engine.*

4.2 Battery and diesel generator sets operating together

4.2.1 Droop control

This control configuration will use droop control of the battery and the generator sets to control the DC-link voltage. The droop controller of the generator sets in this section, will be the same as in section 4.1.4. For the battery, it is desirable that it is not loaded during steady state operation [12]. For the drooping characteristics of the battery, the idle voltage reference needs to be moved towards the reference voltage causing zero output power. This voltage point is the resulting voltage level of the generator set with the highest idle reference voltage V_0. In figure 4.21 the operation principles of this control configuration is illustrated for a situation when the load is decreased from a level p_1 to p_2. Initially in this figure, the idle voltage reference of the battery $V_{0,bat}$ is set to v_2 and it supplies zero power. At the load change to p_2, the droop characteristic of the battery will cause the battery to absorb the power p_{bat}. As $V_{0,bat}$ moves towards v_2, the amount of power the battery absorbs is decreasing towards zero.

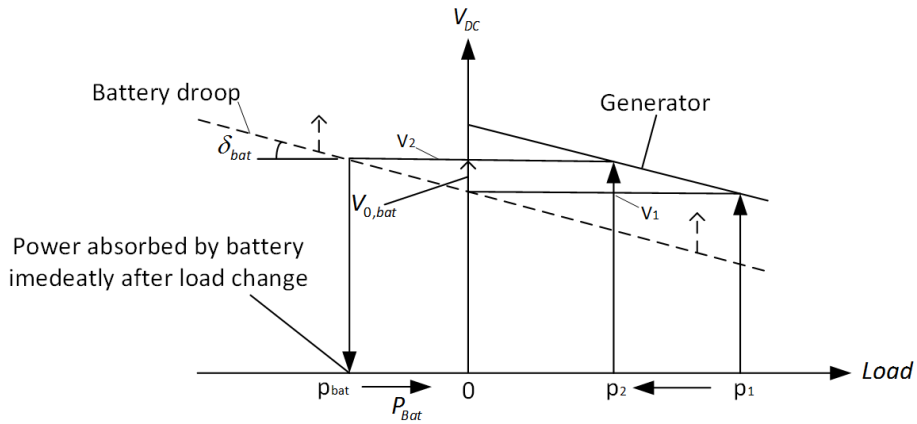

Figure 4.21: *Graphical illustration of battery droop control for a battery and generator operating together.*

Figure 4.22 shows the implemented block diagram of the battery droop controller. The low-pass filter with the time coefficient T_{bat} is used to regulate the rate of which $V_{0,bat}$ will move towards V_{DC}. The larger T_{bat} is, the slower will $V_{0,bat}$ be equal V_{DC} and the battery will be more employed. The slope of the battery droop is set by $delta_{bat}$. V_{max} and V_{min} is set according to keep the DC-link voltage within acceptable ranges.

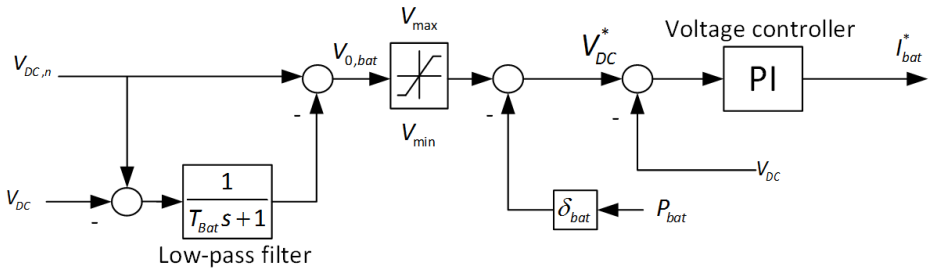

Figure 4.22: *Block diagram battery droop controller*

The selection of δ_{bat} is intrinsic for the instant power exchanged between the battery and the DC-link. From figure 4.21 it can be understood that the smaller δ_{bat} is, the higher share of power will be taken by the battery at load changes. The share of power between the battery and generator sets at a sudden load change P_{tot}, can be obtained by solving the equation set below (see appendix section B.2)

$$-P_{gen1}\delta_1 - P_{gen2}\delta_2 = V_{01} - V_{02} \tag{4.20}$$

$$P_{gen2}\delta_2 - P_{Bat}\delta_{bat} = V_{02} - V_{0,bat} \tag{4.21}$$

$$P_{gen1} + P_{gen2} + P_{bat} = P_{tot} \tag{4.22}$$

Equation 4.20-4.22 cannot precisely be applied to predict the resultant power share of a load change, as distortion of the DC-link voltage and delays will impact. However, it may give knowledge on how the battery will respond to load changes. For the applied $\delta_{bat} = 0.05\,pu$ this is an example: initially the load is $1.33\,pu$ and the battery supplies zero power implying $V_{0,bat} = V_{02}$. If the battery then raises instantaneously to $2\,pu$ equation 4.20-4.21 will result in a instant battery power of $0.3\,pu$.

When the battery is employed, the dynamic response of the power system will become distinctively improved and fast transient action of the generators is not necessary. Regarding selection of T_{Bat} and T_{di}, most even operation of the generator sets is obtained if T_{di} is increased compared to in section 4.1.4 and $T_{bat} < T_{di}$. It is also important to notice that as the battery power proceed towards zero, a load change will be experienced by the generator sets. Hence, if T_{bat} is too small, and battery power reduces too fast, operation of the generators sets may be instable. Control parameters for the battery droop control parameters are given in table 4.5.

$\delta_{bat} = 0.05\,pu$	$T_{bat} = 5$	$T_{di} = 8$	$V_{max} = 1.06\,pu$	$V_{min} = 880\,V$	$V_{max} = 985\,V$

Table 4.5: *Control parameters for droop control of battery and generator sets. Other parameters are the same as in section 4.1.4.*

4.2.2 Performance test battery droop control

When the battery is added in the power system, the power is allowed to raise faster and the filtering time-coefficient of the load is set 1.5 s. When the powers of the battery and the generators sets crosses after 3 s in figure 4.23, more uneven power supply of the generators appears. More voltage ripple appears when the battery power crosses the zero after 12 s. When the load drops to zero, the over-voltage raises from 890 to 1100 V and lasts for approximately 0.1 s (figure 4.24). This is significantly lower than without the battery where voltage levels reached almost 1300 V. The power the battery absorbs reaches 1.1 pu which is tolerable for the battery for a short time (see section 3.4).

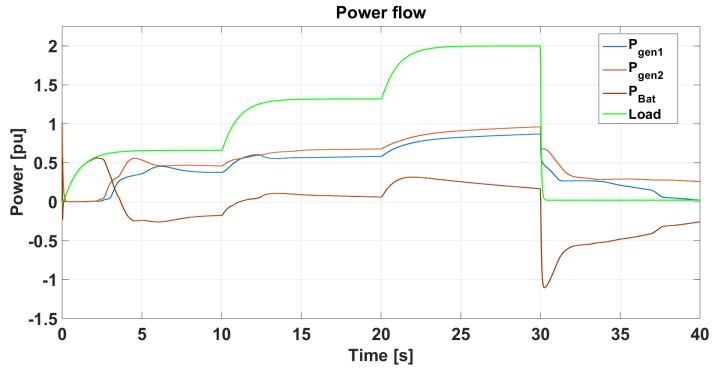

Figure 4.23: *Performance test of droop control of battery and two generator sets: power flow*

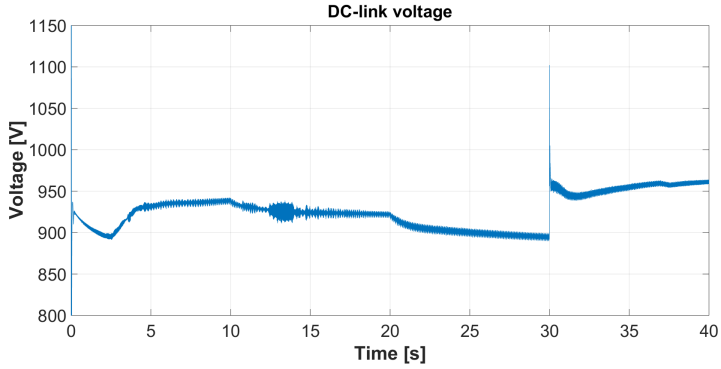

Figure 4.24: *Performance test of droop control of battery and two generator sets: DC-link voltage*

4.2.3 Master slave operation battery and generator sets

In this last control strategy, the DC-link voltage is controlled by the battery, while the diesel generators receive a reference power. This is called master-slave operation. The control structure of the battery will be the same as designed in section 3.4.2 with the nominal DC-link-voltage of $930\,V$ as reference. The field-voltage controllers in the diesel generators will be regulated with the received power reference as control signal. As the DC-link voltage will be kept constant, the power to the generator is translated to a current reference. With equal share of power between the generators, the current reference becomes

$$I^*_{DC} = \frac{P_{load}}{2V_{DC}} \tag{4.23}$$

The maximal current in terms of maximum output torque of the diesel engine can be written as

$$I^*_{DC,max} = \frac{T_{m,max}}{V_{DC}} \tag{4.24}$$

Figure 4.25 shows the block diagram of the current control loop. The low-pass filter with time coefficient will be used to limit current reference to the generator for more steady operation.

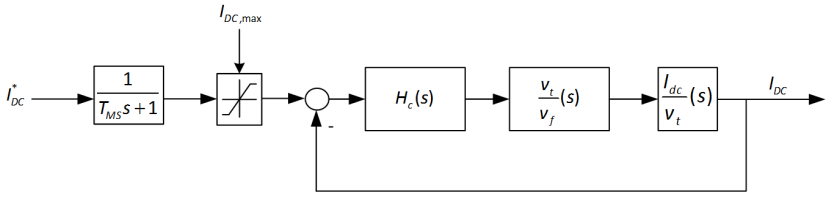

Figure 4.25: *Block diagram of current control of the generator sets*

The control loop of the field voltage controller must therefore be redefined. As the DC-link voltage is kept constant by the battery, the transfer function from output terminal voltage to the output DC-current, the transfer function $\frac{I_{DC}}{V_t}(s)$ for each generator may be investigated. This transfer-function can be framed as follows (see appendix section B.1 for derivation)

$$\frac{I_{DC}}{v_t}(s) = \frac{3\sqrt{2}}{\pi} \frac{\frac{R_{CPL}Cs+1}{R_k+R_{CPL}}}{s^2\frac{R_{CPL}CL_k}{R_k+R_{CPL}} + s\frac{R_{CPL}R_k+L_k}{CR_k+R_{CPL}} + 1} \tag{4.25}$$

In this transfer function time coefficients of the denominator equals t_1 and t_2. $R_{CPL}C = 15ms$. A PI-controller is applied to the control loop. This control case is similar to the DC-link voltage controller in section 4.1.4, and modulus optimum is applied. Hence, T_i cancels out T'_{d0}. The value of K_p has been reduced to avoid instability issues between the generators and the battery. The derivate effect in the numerator of equation 4.25, may be the reason for that as. Reduced stability performance using master-slave is also

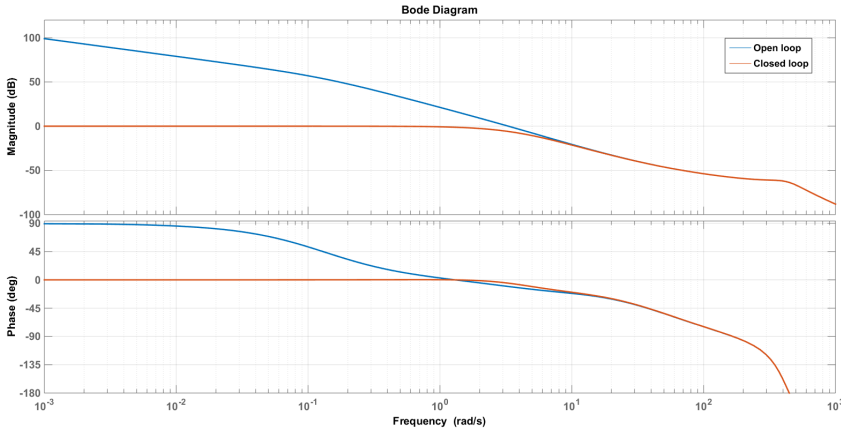

Figure 4.26: *Bode diagram of current-control loop for the generator sets. Bandwidt* : $3.79\,rad/s$. *PM* : $168°$

mentioned in [5]. The bode-plot of the control loop with applied control parameters is shown in 4.26.

Regarding the selection of T_{MS} and T_{di}, experimental testing has shown that $T_{MS} \leq 1\,s$ and T_{di} significantly lower than T_{MS} for better operation of the generator sets. Table 4.6 summarizes control parameters for the master-slave configuration.

$K_p = 10$	$T_i = 7.55$	$T_{MS} = 2$	$T_{di} = 10$

Table 4.6: *Control parameters for the master-slave configuration*

4.2.4 Performance test master slave

Since the generator sets are implemented with the same settings and supply the same amount of power, their waveforms in figure 4.27 are also identically. The oscillations in the generator wave-form occurring after $15\,s$ would have been larger with higher K_p in the current controller. Compared to the battery droop controller, the implemented configuration gives slower response of the generator sets causing the battery to be more stressed. When the load drops to zero, the battery nearly supplies $2\,pu$. In figure 4.28, the DC-link voltage can be seen stable regulated at the nominal value of $930\,V$. The over-voltage raises to $1100\,V$, which is a lower skip than with the battery droop controller.

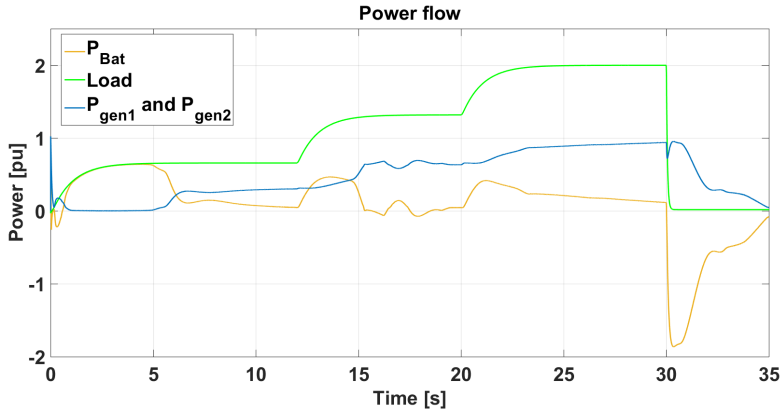

Figure 4.27: *Performance test master slave configuration: power flow. The wave-form of the generator sets is identically.*

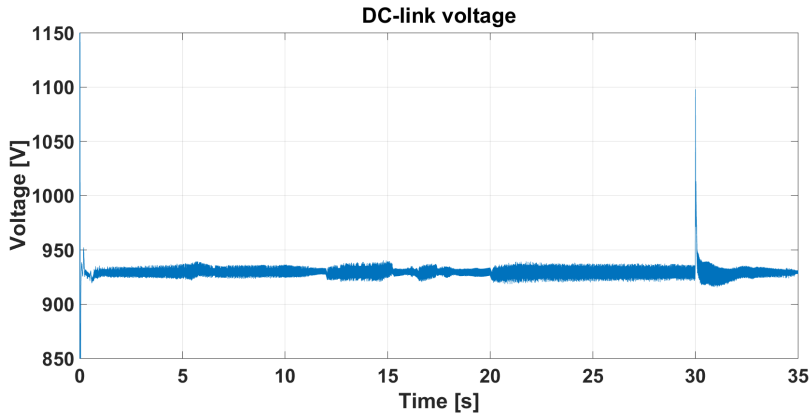

Figure 4.28: *Performance test master slave configuration: DC-link voltage*

4.3 Overall evaluation of control structures

The variable speed operation of generator sets is a factor that causes the power system to be more sensitive to instability. In this sense, increasing T_{di} sufficiently, in order to lower the bandwidth of the speed control loop, is a key to stable operation. Moreover, is the generators in the dual operation highly exposed to each other. Instability in one generator affects the other.

The single voltage control-loop displays good voltage-response and stable power-flow of the generator set. However, this control-structure has low bandwidth. A controller of higher bandwidth would be desired to limit over-voltage at drop out of load. Compared with employment of battery, the resulting over-voltage is considerably higher. An exciter-system with lower τ_{ex} would have allowed higher bandwidth since ω_{180} would be higher.

The cascaded control-scheme is designed with distinctively higher bandwidth of the inner-loop than of the single voltage-controller. This is necessary in order to obtain decent bandwidth of the outer-loop. Simulation results showed that this structure is highly instable. Also when the speed is fixed, there are steady oscillations in output power. It may be that the higher bandwidth of the inner controller is not tolerable in the situation of the dual operation of the generators. A known issue is also that the derivative effect may gain up disturbances. In this context, effects of the commutation process should be more deeply investigated as this causes steady variations in generator inductances. It could therefore be of interest to check the performance of the inner-loop controller for a power system without diode-bridge.

The power controller added in the speed controller in section 4.1.8, proved to allow faster load changes as well as it yields more stable output-power of the generators. The reason for this improvement, might be explained by the torque characteristic of the diesel engines. When the engine speed of the generators are different and below $0.8\,pu$, the maximum torque of the engines also are different according to equation 3.26. This results in different acceleration and maximum output power of diesel engines, which is reflected in oscillations in output power. By adding the power controller, differences in rate of change in engine speeds are even out. This theory is supported, by the oscillations appearing in figure 4.7 in the load change from 0.66 to $1.33\,pu$ when speed is below $0.8\,pu$. In the load change from $1.33\,pu$ to $2\,pu$, when speed is above $0.8\,pu$, acceleration in engine speed as well as output power proceeds steadily. Besides improved dynamic response with respect to load changes, the power controller can be useful if it allows the size of capacitor in the DC-link to be reduced. Strategies for improved stability and reduction of the capacitor in the DC-link of a HPS is an addressed topic in [26, p. 77].

When the battery is introduced in the power system, the ability to supply transient load is improved as well as more stable power waveform of the generator sets are obtained. This is due to the high bandwidth of the battery-controller. Of the two implemented load-sharing strategies, the battery droop-controller has more parameters to tune compared to the master-slave configuration. This makes the battery droop-controller more intricate

to implement. Instead of a dynamic droop controller, a constant droop-controller equal to that of the generators could be designed. In this case, equation 4.20 - 4.22 easily can be used to obtain a reasonable power share between battery and generator sets. The battery-droop controller might be more redundant if the battery is tripping. With the master-slave configuration, it will in this case be no control of the DC-link voltage. As will be seen in the next chapter, master-slave has the advantage that output power of the generator set can be set to a specific level.

5 | Simulation of a driving profile - evaluation of fuel consumption

A driving profile for the power system is set up based on the dimensioning load profile in section 3.1.1. The load point from 200 to 450 s are used and fitted into a adequate simulation time of 45 s which makes the water slightly "rougher". The driving profile is simulated with five different control cases where the generator sets either are operating alone or with the battery. Definition and settings of each control case is listed below:

Case 1 Generator set operating alone with fixed maximum speed. Droop control structure of generator set with settings equal to section 4.1.4.

Case 2 Generator set operating alone. Droop control structure of generator set. Control settings equal to section 4.1.4.

Case 3 Generator set operating alone. Power controller added to diesel engine. Settings equal to section 4.1.8.

Case 4 Generator set and battery operating together. Droop controller of battery. $T_{di} = 10$ and $T_{Bat} = 6.25$. Other settings are equal to section 4.2.1.

Case 5 Generator set and battery operating together. Master-slave control structure. Generator sets are adjusted to supply a power of 0.82 pu which approximately is the operating point at which generator sets display highest efficiency. Other settings are equal to section 4.2.3.

The aim of the simulations is to illustrate applications of controller structures and moreover to estimate the fuel consumption of diesel. Based on estimated fuel consumption, feasibility of each case, with reference to the fixed speed operation in case 1, will be assessed.

To obtain an expression of fuel consumption the, implemented script for calculation of SFOC will be used. The total mean SFOC including both generators is calculated by

$$\overline{SFOC} = \frac{\int_0^t SFOC_{gen1}(t) + SFOC_{gen2}(t)dt}{2t} \tag{5.1}$$

The diesel weight in gram/liter is assumed for marine diesel oil to 855 [gr/l] [59]. The mean diesel consumption per hour is then obtained by

$$Mean\,diesel\,consumption\,[l/h] = \frac{\overline{SFOC}\,[gr/kWh] \cdot P_{avg}\,[kW]}{855\,[gr/l]} \tag{5.2}$$

When the generators set are operating alone, P_{avg} is the time averaged load which is calculated to $1131.4kW$ $(1.4\,pu)$ for the driving profile. When the battery is added, the generator sets will supply P_{avg} in addition to the losses in battery and in the battery converter. The mean battery conversion losses are calculated in 5.3. In the simulation cases with battery, the generator set will actually not supply the average load. However, as battery must be charged and discharged, the generator set must on an average basis supply the average load. A more correct way to asses fuel consumption would therefore be to simulate a total charge/discharge cycle of the battery with equal state of charge in the beginning and the end. With a plug-in configuration of the battery, the generator set would not needed to supply the average load.

$$\overline{P_{loss}} = \frac{\int_0^t |P_{bat} - P_{bat}^{in}|dt}{t} \tag{5.3}$$

The term $|P_{bat} - P_{bat}^{in}|$ denotes the absolute value between the battery power and the power into the converter from the DC-link side. To estimate the daily fuel consumption costs, the marine diesel oil price is assumed $7.94NOK/l$, hence

$$Fuel\,costs\,[NOK/day] = Mean\,diesel\,consumption\,[l/h] \cdot 7.94\,[NOK/l] \cdot 24h \tag{5.4}$$

For each simulation case, generator speed and the power flow showing power from battery, generator set and load (driving profile) will be depicted.

5.1 Simulation Case 1 - fixed speed operation

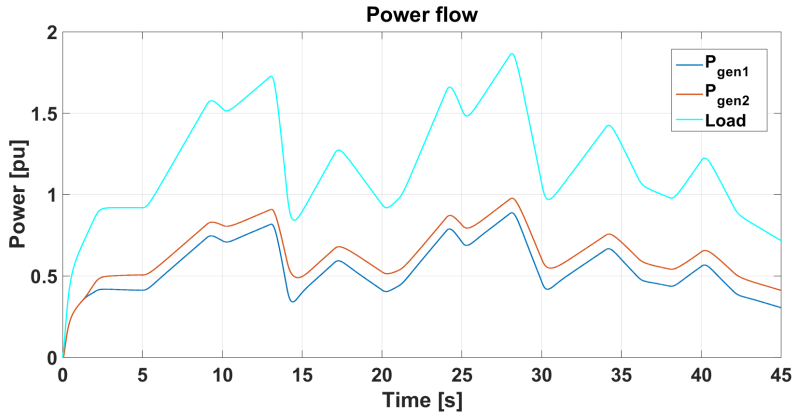

Figure 5.1: *Case 1: Power flow*

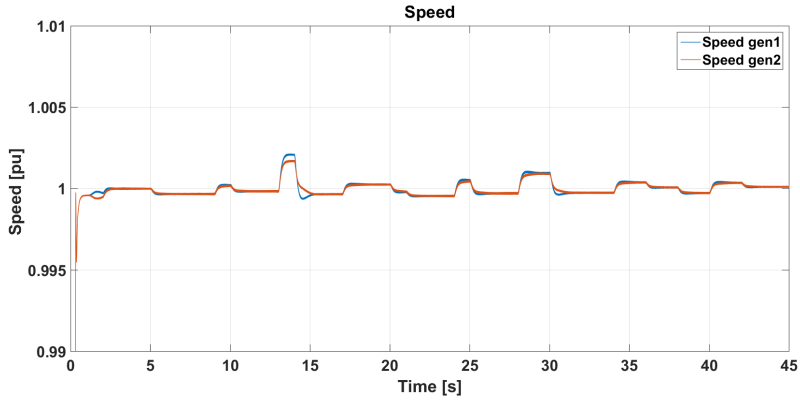

Figure 5.2: *Case 1: engine speed of generator sets. The speed does not deviate much from the reference at* $1\,pu$ *at load changes*

5.2 Simulation Case 2 - variable speed

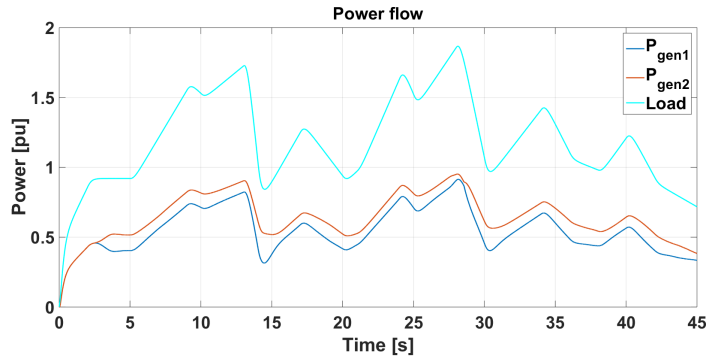

Figure 5.3: *Case 2: power flow*

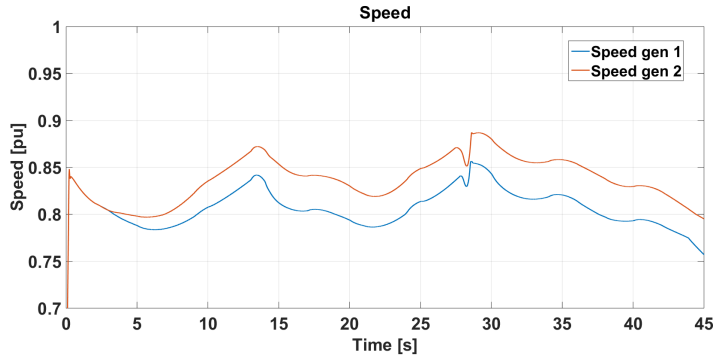

Figure 5.4: *Case 2: speed of generator sets. The load increase after 25s, causes a speed drop and unbalance in the power supply between the generators.*

5.3 Simulation Case 3 - variable speed and power controller added to diesel engine

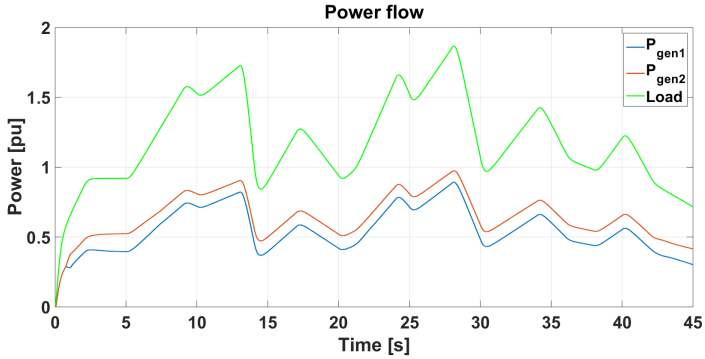

Figure 5.5: *Case 3: power flow. The power waveforms of the generator can be seen to proceed slightly more smoothly when the power controller is added to the diesel engine.*

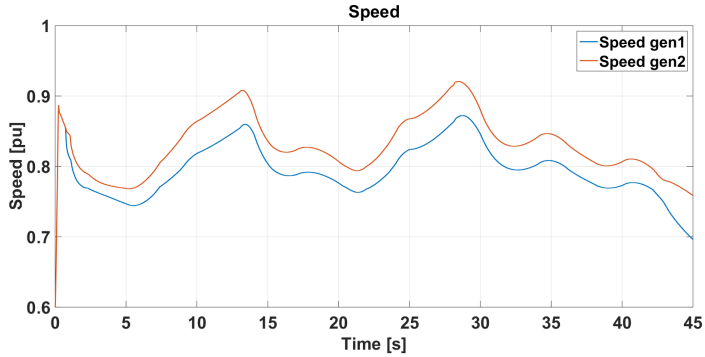

Figure 5.6: *Case 3: speed of generator sets.*

5.4 Simulation results Case 4 - droop control with generator set and battery

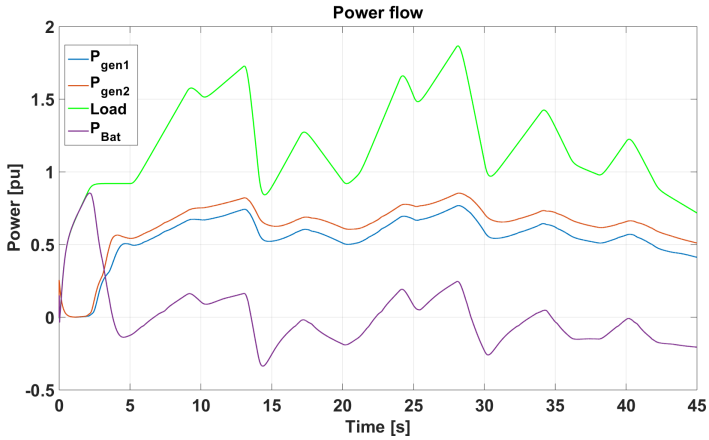

Figure 5.7: *Case 4: power flow.*

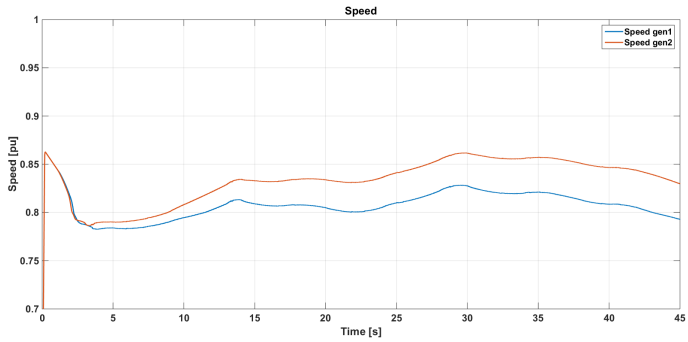

Figure 5.8: *Case 4: speed of generator sets.*

5.5 Simulation results Case 5 - generator sets and battery operating together with master-slave control structure

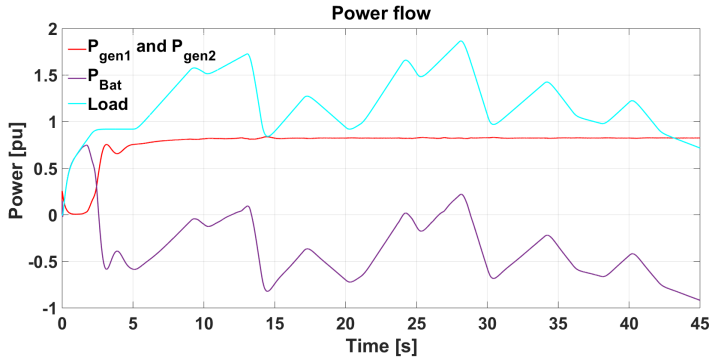

Figure 5.9: *Case 5: power flow. Since both generator set supply the same load, the waveforms of the generator sets are identical.*

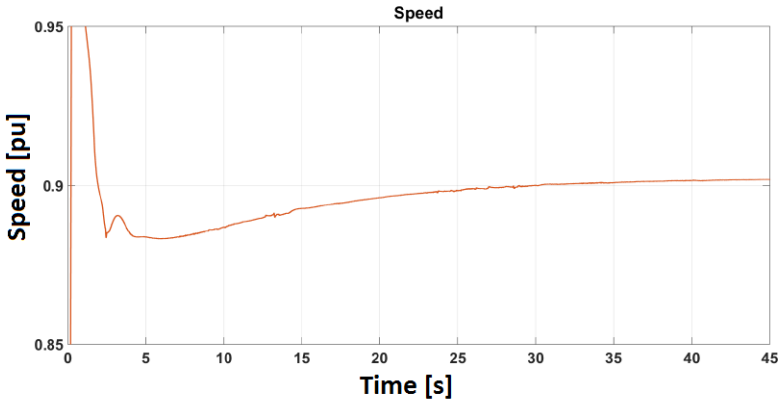

Figure 5.10: *Case 5: speed of generator sets. Due to a large T_{di} in the diesel engine the speed is very slowly proceeding towards a steady value*

5.6 Assessment of fuel consumption

For a better understanding of how SFOC varies during the simulation, the SFOC-waveforms have been plotted together as depicted in figure 5.11. It can be seen from this figure that for Case 1, the SFOC is generally higher. When generator sets supply less power, the SFOC rapidly increases. Case 2 and Case 3 have almost identical waveforms. In table 5.1, calculations and consequences of fuel consumption are summarized.

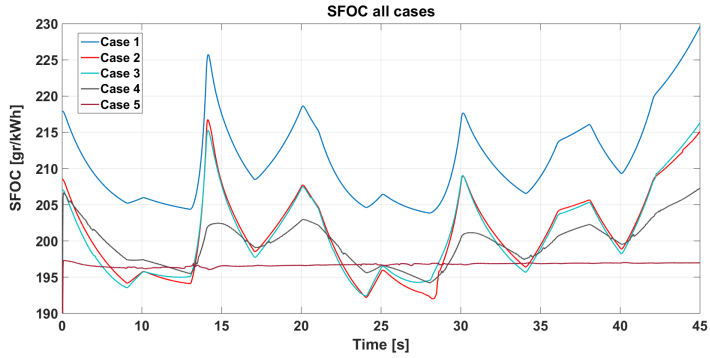

Figure 5.11: *Waveworm of SFOC for all cases plotted together*

	Case 1	Case 2	Case 3	Case 4	Case 5
Mean battery + converter losses [kW]				0.501	3.5
Mean SFOC [gr/kWh]	211.9	201.9	201.55	199.75	196.7
Mean Diesel consumption [liter/hour]	280.3	266.71	266.6	264.34	260.99
Fuel costs [NOK/day]	53 415	50 894	50 806	50 374	49 734

Table 5.1: *Summary of calculations from simulated cases.*

From the daily fuel costs in table 5.1, yearly fuel savings of each case with respect to fixed in Case 1, is calculated in table 5.2

Fuel cost saving per year with respect to fixed speed

Case 2	**Case 3**	**Case 4**	**Case 5**
92 0165 NOK/year	95 2285 NOK/year	1 109 965 NOK/year	1 343 565 NOK/year

Table 5.2: *Yearly fuel savings for Case 2-Case 5 with respect to fixed speed operation in Case 1*

Assuming the battery back has a cost of 3 000 000 NOK (actual prices of the Corvus battery were not available), payback time of the battery can be calculated based on the

daily fuel cost savings. Table 5.3, shows payback time of battery bank for Case 4 and Case 5 with respect to fixed speed - Case 1 and variable speed - Case 2.

Payback time battery

	Case 4	**Case 5**
Fixed speed - Case 1	2.7 years	2.23 years
Variable speed - Case 2	15.8 years	7.08 years

Table 5.3: *The table shows the payback time of the battery as simulated in Case 4 and Case 5 with respect to simulations without battery in Case 1 and Case 2.*

5.7 Overall evaluation of fuel consumption

Estimations of fuel consumption from the particular driving profile simulated in this chapter, confirm that variable speed operation has potential to yield intrinsic fuel and cost savings over time. This presupposes that the load profile is of varying character, as low load causes rapidly raise of SFOC at fixed speed operation.

Comparing Case 2 and Case 3, fuel consumption in Case 3 are slightly lower than in Case 2 according to table 5.1. This small difference may be a causality for the particular driving profile, but with the power controller added, fuel can potentially be reduced as this control structure provides faster dynamic. That is, the optimal speed reference will be tracked faster. However, the contribution from the power controller, is not tuned in order to give optimal speed. Hence, this additional contribution to the speed reference, may distort the optimal speed reference. As the driving profile in the simulations has been made more steep than in reality, the power controller will most likely not be necessary. The regular speed controller will in that sense have sufficient dynamic. If stability issues between the generator should occur or more extreme load changes were subjected to the generator sets, power controller of the engine speed could be considered.

When the battery is added in Case 4 and Case 5, the strength of the hybrid power system is illustrated as the load subjected to the generator sets becomes more steady. The master-slave configuration in Case 5, has the advantage that load supplied by generator sets easily can be adjusted to yield minimum fuel consumption. However, this operation causes more stress on the battery. In figure 5.9 it can be seen that the battery power nearly reaches $-1\,pu$. When the generator sets supply a mean average load as in Case 4, the battery stress will be reduced. With this operation of the generator sets, the battery bank could be dimensioned with lower power ratings, as the generator sets contribute in supplying load fluctuations. In the end of the simulation when the load falls below $1\,pu$, SFOC in Case 4 rapidly increases. If load would stabilize at this low level, it would be natural to have only one generator operating together with the battery. Also, if the battery would be fully charged, one generator should be turned off.

Considering payback time of the battery bank, it will according to table 5.3, within few years bring return compared to fixed speed operation. Compared to a variable speed operation, economic profit is not guaranteed. For Case 4 and Case 5 the payback time is 15.8 and 7.08 years respectively. Depending on how much stress is exerted on the battery, the battery bank might then be substituted before payback time is reached.

A significant weakness of the model used to calculate SFOC of generator set, is that it does not account for transient operation in the diesel engine. Load fluctuation and speed variations, is as mentioned in section 2.2, is a source of increased SFOC as well as maintenance of the diesel engine. The validity of the fuel consumption data presented in this section is therefore, only valid in a steady state operation. In this review, the profit of installing a battery bank may be even more significant due to more stable power supplied by the generator sets. The rate of change at which the engine speed can be allowed to vary should also be discussed in this context. Concerning the oscillating torque-characteristic of the synchronous generators due to the commutation in the diode bridge, it would be interesting to investigate whether these oscillations have an impact on the fuel consumption.

6 | Conclusion

In this master thesis, dimensioning and construction of a DC-grid hybrid power system, with battery and variable speed disesel generators, is thoroughly outlined through simulation models in Matlab/Simulink. Operation of the generator sets alone and together with the battery is investigated. Both cases are addressed with respect to control structures and fuel consumption.

For operation of generator sets alone, two different exciter-voltage control structures with droop control of generator sets are designed. By using a single PI-controller to control the DC-link voltage, stable power-waveforms of generator sets as well as good voltage response in the DC-link is obtained. The second exciter-voltage controller is modeled as a cascaded controller, controlling the terminal and DC-link voltage. Since, the inner-loop would yield low bandwidth using PI-controller, a PID-controller is considered. In the outer-loop a PI-controller is used. This control structure results in oscillations in the output power of the generator sets.

A main factor to obtain stability with variable speed operation, is feeding the speed reference to the speed controller with distinctively lower bandwidth than the voltage controller. This, slows down transient response of the generator sets. By a proposed power-controller added to the speed-controller, load is allowed to increase faster and more stable output power of the generator sets is obtained.

For operation of generator sets and battery together, two control strategies for the load share between generator sets and battery are designed. By using droop control of battery and generator sets, it is shown how the battery droop controller can be designed in order to yield zero battery power in steady state. The second strategy is a master-slave configuration where the battery keeps the DC-link voltage steady. This strategy has the advantage that the generator sets easily can be set to supply optimal power.

The fuel consumption of diesel engines are estimated by a SFOC-model which is based on stationary operation with respect to engine speed and engine load. With generator sets operating alone, this SFOC-model predict large fuel savings for operation on variable speed. The same is proved when battery is added, which also is confirmed by existing hybrid power systems. Comparing the operation modes, generator sets operating alone with variable and operation with battery, the advantage in terms of fuel savings is not obvious. However, as the SFOC-models used does not account for transient operation of the diesel engine, it remains as an uncertainty to which extend the battery is profitable compared to alone-operation of generator set with variable speed.

6.1 Further work

The hybrid power system with associated control structures developed in this thesis comprises a framework which can be applied to further investigation and improvements of control structures as well as in analysis of fuel consumption.

Regarding voltage controllers of generator sets, it should be intended to develop voltage controllers that are faster and reduce over-voltage as a consequence of load drop-out. In this regard, better understanding of generator sets with respect to effects of commutation in the diode bridge can be addressed.

It is of highly interest to develop better models for estimation of fuel consumption in diesel engines, which also takes transient operation into consideration. In combination with a decay-model of Li-ion batteries, an accurate estimation of fuel consumption will comprise a powerful tool to assess the feasibility of the hybrid system. Concerning evaluation of SFOC in this thesis, through cases with and without battery, the feasibility of the following operation modes would be of interest to investigate more:

- Most feasible operation with battery, fixed optimal load or average load supplied by generator sets.
- Most feasible operation of using battery versus generator sets operating alone with variable speed.
- When generator sets are operating alone, the most feasible operation of variable speed versus fixed speed.

Bibliography

[1] IMO. Low carbon shipping and air pollution control, May 2016. http://www.imo.org/en/MediaCentre/HotTopics/GHG/Pages/default.aspx.

[2] Technology, December 2015. http://vikinglady.no/technology/.

[3] Dean Slavnich. Electric pioneer. *Elerctric hybrid - marine technology international*, pages 4–8, Oct 2015. http://viewer.zmags.com/publication/061eea2c#/061eea2c/6.

[4] ABB. Onboard dc grid. *ABB*, 2011.

[5] Ac-microgrids versus dc-microgrids with distributed energy resources: A review. *Renewable and Sustainable Energy Reviews*, 24:387 – 405, 2013.

[6] Jean-Frederic Charpentier Jingang Han and Tianhao Tang. An energy management system of a fuel cell/battery hybrid boat. *Energies 7*, pages 2799–2820, 2014.

[7] Souleman Njoya Motapon. A comparative study of energy management schemes for a fuel-cell hybrid emergency power system of more-electric aircraft. *IEEE*, 2013.

[8] David C. Yu Amin Hajizadeh, Amir Hossein Shahirinia. Fuzzy control of supercapacitor current in hybrid diesel generator/fuel cell marine power system. *Journal of Fuel Cell Science and Technology*, 2015.

[9] Assessing the potential of hybrid energy technology to reduce exhaust emissions from global shipping. *Energy Policy*, 40:204 – 218, 2012.

[10] DNV-Gl. In focus the future is hybrid, 2015. https://www.dnvgl.com/Images/DNV%20GL%20In%20Focus%20Battery_tcm8-24901.pdf.

[11] I. Chotia and S. Chowdhury. Battery storage and hybrid battery supercapacitor storage systems: A comparative critical review. In *Smart Grid Technologies - Asia (ISGT ASIA), 2015 IEEE Innovative*, pages 1–6, 2015.

[12] R. Nilsen and I. Sorfonn. Hybrid power generation systems. In *Power Electronics and Applications, 2009. EPE '09. 13th European Conference on*, pages 1–9, 2009.

[13] FellowSHIP. Fellowship iii - hybridship, May 2016. http://vikinglady.no/wp-content/uploads/2012/03/HybridShipPresentation.pdf.

[14] Bu-808: How to prolong lithium-based batteries. http://batteryuniversity.com/learn/article/how_to_prolong_lithium_based_batteries.

[15] Battery univerity. What is c-rate?, May 2016. http://batteryuniversity.com/learn/article/what_is_the_c_rate.

[16] A.E. Trippe, R. Arunachala, T. Massier, A. Jossen, and T. Hamacher. Charging optimization of battery electric vehicles including cycle battery aging. In *Innovative Smart Grid Technologies Conference Europe (ISGT-Europe), 2014 IEEE PES*, pages 1–6, 2014.

[17] Maria Teresa Troncoso Abelleira. Batteries for marine applications. Master thesis, Norwegian University of Science and Technology, Department of Marine Technology, 2013.

[18] Huirong Jiang Xiangjiang Yang and Zhicheng Deng. Design of a battery management system based on matrix switching network. In *Information and Automation, 2015 IEEE International Conference on*, pages 138–141, 2015.

[19] DNV-Gl. Dnv gl guideline for large maritime battery systems, March 2014.

[20] Lithium-ion batteries for off-grid systems, are they a good match?, jan 2016. `http://www.homepower.com/articles/solar-electricity/equipment-products/lithium-ion-batteries-grid-systems?v=print`.

[21] Battery technology charges ahead, Jul 2012. `http://www.mckinsey.com/insights/energy_resources_materials/battery_technology_charges_ahead`.

[22] Bu-1003: Electric vehicle (ev), Jan 2016. `http://batteryuniversity.com/learn/article/electric_vehicle_ev`.

[23] Bu-205: Types of lithium-ion, Jan 2016. `http://batteryuniversity.com/learn/article/types_of_lithium_ion`.

[24] Corvus energy storage system - ess, Jan 2016. `http://corvusenergy.com/energy-storage-system/`.

[25] Bo Liang, Yanping Liu, and Yunhua Xu. Silicon-based materials as high capacity anodes for next generation lithium ion batteries. *Journal of Power Sources*, 267:469 – 490, 2014.

[26] Bijan Zahedi. Shipboard dc hybrid power systems. Doctoral thesis, Norwegian University of Science and Technology, Department of Marine Technology, 2014.

[27] J. Jatskevich, S. D. Pekarek, and A. Davoudi. Parametric average-value model of synchronous machine-rectifier systems. *IEEE Transactions on Energy Conversion*, 21(1):9–18, 2006.

[28] Electric and hybrid marine world expo patrick baan, April 2016. `http://www.slideshare.net/wartsilacorp/electric-and-hybridmarineworldexpopatrickbaan062014`.

[29] D. Browningb Q. Caia, D.J.L. Bretta and N.P. Brandon. A sizing-design methodology for hybrid fuel cell power systems and its application to an unmanned underwater vehicle. 2010.

[30] K. Varesi and A. Radan. A novel pso based technique for optimizing the doh in hybrid electric vehicles to improve both the fuel economy and vehicle performance and reduce the emissions. In *Power Electronics, Drive Systems and Technologies Conference (PEDSTC), 2011 2nd*, pages 342–349, 2011.

[31] A. M. Rahimi and A. Emadi. Active damping in dc/dc power electronic converters: A novel method to overcome the problems of constant power loads. *IEEE Transactions on Industrial Electronics*, 56(5):1428–1439, 2009.

[32] A. Emadi, A. Khaligh, C. H. Rivetta, and G. A. Williamson. Constant power loads and negative impedance instability in automotive systems: definition, modeling, stability, and control of power electronic converters and motor drives. *IEEE Transactions on Vehicular Technology*, 55(4):1112–1125, 2006.

[33] MathWorks. Synchronous machine, May 2016. http://se.mathworks.com/help/physmod/sps/powersys/ref/synchronousmachine.html;jsessionid=

[34] Nokian Capacitors. Rectifierscomp, Feb 2016. `http://www.rww.co.za/downloads/Harmonics_and_Reactive_Power_Compensation_in_Practice.pdf`.

[35] A. Al-Busaidi and V. Pickert. Comparative study of rectifier circuits for series hybrid electric vehicles. In *Hybrid and Eco-Friendly Vehicle Conference, 2008. IET HEVC 2008*, pages 1–6, 2008.

[36] W.P Robbins Ned Mohan, T.M Undeland. *Power Electronics - Converters, Applications and Design*. Wiley, 2003.

[37] S. Moriyasu and C. Uenosono. An analysis on the characteristics of a synchronous machine connected to a d.c.-link. *Archiv für Elektrotechnik*, 69(2):111–120.

[38] Prabha Kundur. *Power System Stability and Control*. McGraw-Hill, Inc, 1994.

[39] A. Ula and A. R. Hasan. Design and implementation of a personal computer based automatic voltage regulator for a synchronous generator. *IEEE Transactions on Energy Conversion*, 7(1):125–131, 1992.

[40] Roy Nilsen. *SIE2025 Elektriske motordrifter*. NTNU, 2000.

[41] B. Zahedi and L. E. Norum. Modelling and simulation of hybrid electric ships with dc distribution systems. In *Power Electronics and Applications (EPE), 2013 15th European Conference on*, pages 1–10, 2013.

[42] Ø.N Smogeli. *Control of Marine Propellers: From Normal to Extreme Conditions*. PhD thesis, Marine Technology, Norwegian University of Science and Technology, 2006.

[43] A ship propulsion system as a benchmark for fault-tolerant control. *Control Engineering Practice*, 7(2):227 – 239, 1999.

[44] Bjarne A. Foss Jens G. Balchen, Trond Andresen. *Reguleringsteknikk*. Institutt for teknisk kybernetikk, 2003.

[45] B. Zahedi and L. E. Norum. Efficiency analysis of shipboard dc power systems. In *Industrial Electronics Society, IECON 2013 - 39th Annual Conference of the IEEE*, pages 689–694, 2013.

[46] Olivier Tremblay. Experimental validation of a battery dynamic model for ev applications. *World Electric Vehicle Journal Vol. 3*, 2009.

[47] Corvus Energy. Corvus energy storage system, May 2016. `http://corvusenergy.com/energy-storage-system-html/`.

[48] MathWorks. Battery, May 2016. http://se.mathworks.com/help/physmod/sps/powersys/ref/batte

[49] Alireza Safaee Praveen Jain Alireza Bakhshai Hamid R. Karshenas, Hamid Daneshpajooh. Bidirectional dc-dc converters for energy storage systemss. *Energy Storage in the Emerging Era of Smart Grids,*, 2011.

[50] MathWorks. Pwm generator (dc-dc), May 2016. http://se.mathworks.com/help/physmod/sps/powersys/ref/pwmgeneratordcdc.html.

[51] J. Wang, K. Zou, C. Chen, and L. Chen. A high frequency battery model for current ripple analysis. In *Applied Power Electronics Conference and Exposition (APEC), 2010 Twenty-Fifth Annual IEEE*, pages 676–680, 2010.

[52] Sven De Breucker. Impact of dc-dc converters on li-ion batteries. Doctoral thesis, Katholieke Universiteit Leuven – Faculty of Engineeringy, 2012.

[53] Emerson Network Power. Effects of ac ripple current on vrla battery life, May 2016. `http://www.emersonnetworkpower.com/documentation/en-us/brands/liebert/documents/white%20papers/effects%20of%20ac%20ripple%20current%20on%20vrla%20battery%20life.pdf/`.

[54] Steven Keeping. Design trade-offs when selecting a high-frequency switching regulator design trade-offs when selecting a high-frequency switching regulator, May 2012. `http://www.digikey.com/en/articles/techzone/2015/feb/design-trade-offs-when-selecting-a-high-frequency-switching-regulator`.

[55] B. Zahedi, O. C. Nebb, and L. E. Norum. An isolated bidirectional converter modeling for hybrid electric ship simulations. In *2012 IEEE Transportation Electrification Conference and Expo (ITEC)*, pages 1–6, 2012.

[56] Roy Nilsen. *Electric Drives. Lecture Notes.* NTNU, 2016.

[57] Q. Shafiee, T. Dragicevic, J. C. Vasquez, and J. M. Guerrero. Modeling, stability analysis and active stabilization of multiple dc-microgrid clusters. In *Energy Conference (ENERGYCON), 2014 IEEE International*, pages 1284–1290, 2014.

[58] J. M. Guerrero, J. C. Vasquez, J. Matas, L. G. de Vicuna, and M. Castilla. Hierarchical control of droop-controlled ac and dc microgrids x2014;a general approach toward standardization. *IEEE Transactions on Industrial Electronics*, 58(1):158–172, 2011.

[59] Cricle K. Priser for bedriftsmarkedet - marinegassolje. ://www.bunkeroil.no/produkter.

Appendices

A | System modeling

A.1 Parameters diesel generator

Parameters synchronous generator

$P_{gen,n} = 800\,kW$	$V_{LL,n} = 690\,V$	$f_n = 50\,Hz$	$p = 6$
$R_s = 0.0026\,pu$	$R_f = 0.00058\,pu$	$R_D = 0.015\,pu$	$R_Q = 0.0151\,pu$
$L_d = 1.379\,pu$	$L_q = 0.773\,pu$	$L_f = 1.3762\,pu$	$L_D = 1.3076\,pu$
$L_Q = 0.712\,pu$	$L_\sigma = 0.107\,pu$	$L_{ad} = 1.2720\,pu$	$L_{aq} = 0.6660\,pu$
$L''_d = 0.13\,pu$	$L''_q = 0.15\,pu$		

Table A.1: *Parameters of the synchronous generator*

Parameters diesel engine

$P_{di,n} = 880\,kW$	$n_n = 1000\,rpm$	$J_{eq} = 42.4\,kg.m^2$	$N = 6$
$C_r = 0.01289$	$K_y = 1$	$H = 0.26\,s$	

Table A.2: *Parameters of the diesel engine*

A.2 Per-unit calculation of synchronous generator

Equation A.1-A.5 show the base value calculation used for the per-unit model of the synchronous machine. Regarding the input of the field voltage, it is normalized with respect to nominal field voltage so that a 1 input produces a $1\,pu$ stator voltage at no load [33].

$$V_{base} = V_{LL,n} \tag{A.1}$$

$$I_{base} = \frac{P_{gen,n}\sqrt{2}}{V_{LL}} \tag{A.2}$$

$$Z_{base} = \frac{V_{LL,n}}{P_{gen,n}} \tag{A.3}$$

$$\omega_{el,base} = 2\pi f_n \tag{A.4}$$

$$L_{base} = \frac{Z_{base}}{\omega_{base}} \tag{A.5}$$

$$\tag{A.6}$$

A.3 Developed Simulink models

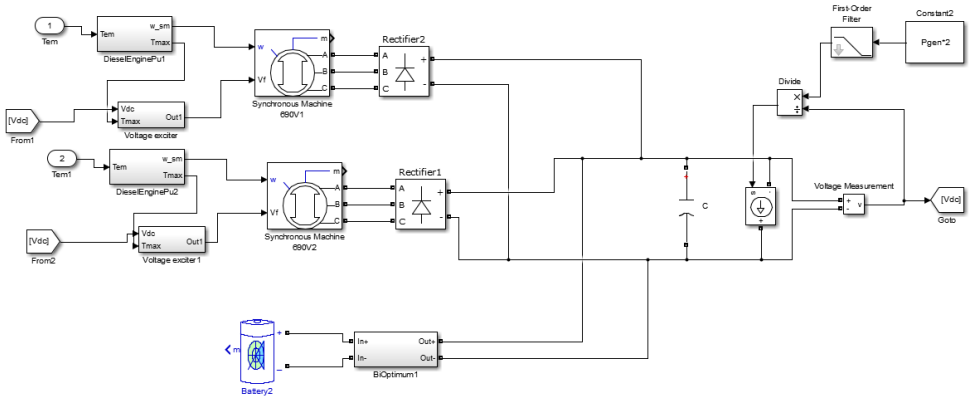

Figure A.1: *Simulink model of the hybrid power system*

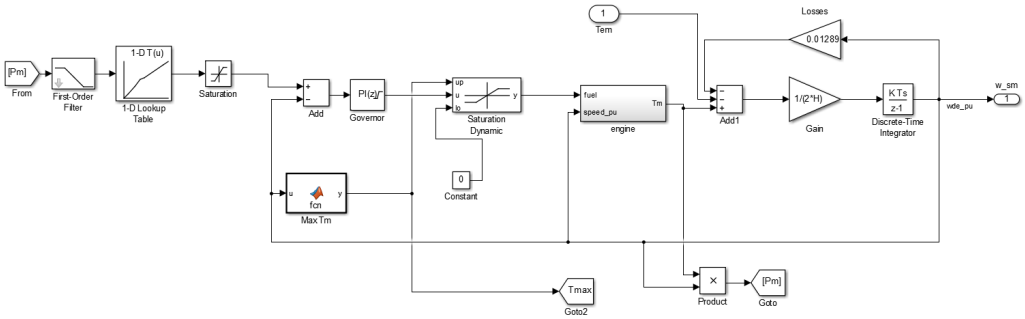

Figure A.2: *Simulink model of the diesel engine*

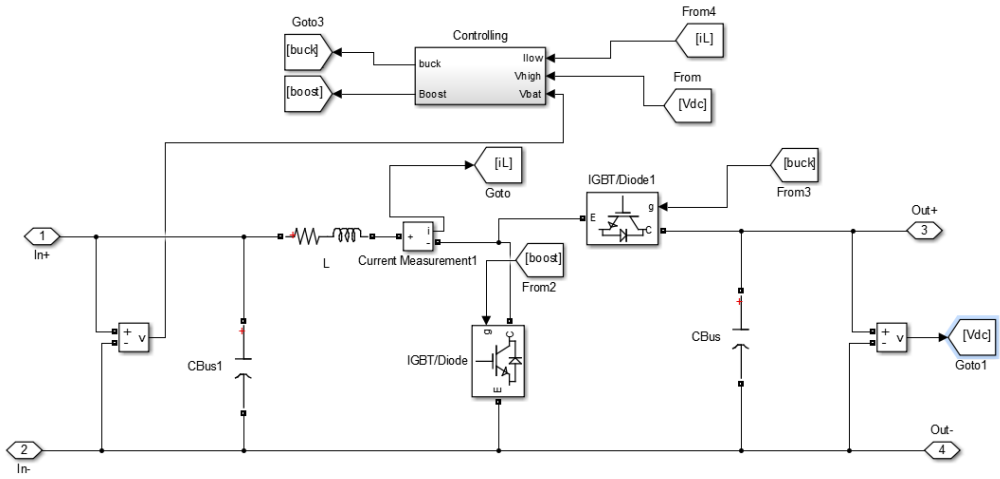

Figure A.3: *Simulink model of the battery converter*

```
function E = SFOC(p,w)
%#codegen
coff=[19.1 164.9 19.54;14.76 172.23 6.92;9.62 189.84 -14.33;5.5 215.68 -51.5;1.8 238.35 -76.75]; %coefficient matrix of support points
if (w>=1)
    E=fuel(coff(1,1),coff(1,2),coff(1,3),p);
elseif (w<1 & w>=0.9)
        y1=fuel(coff(1,1),coff(1,2),coff(1,3),p);       %input interpolation/ calculation of gr/h at w=1 pu
        y0=fuel(coff(2,1),coff(2,2),coff(2,3),p);       %input interpolation/ calculation of gr/h at w=0.9 pu
        E=interPo(y0,y1,0.9,1,w);                       % Interpolation
elseif (w<0.9 & w>=0.8)
    y1=fuel(coff(2,1),coff(2,2),coff(2,3),p);
    y0=fuel(coff(3,1),coff(3,2),coff(3,3),p);
     E=interPo(y0,y1,0.8,0.9,w);
elseif (w<0.8 & w>=0.7)
   y1=fuel(coff(3,1),coff(3,2),coff(3,3),p);
   y0=fuel(coff(4,1),coff(4,2),coff(4,3),p);
   E=interPo(y0,y1,0.7,0.8,w);

elseif (w<0.7 & w>=0.6)
   y1=fuel(coff(4,1),coff(4,2),coff(4,3),p);
   y0=fuel(coff(5,1),coff(5,2),coff(5,3),p);
   E=interPo(y0,y1,0.6,0.7,w);
elseif (w<0.6)
    E=fuel(coff(5,1),coff(5,2),coff(5,3),p);
end
E=E/p; %into SFOC [gr/kWh]
end
```

Figure A.4: *Matlab script for calculation of SFOC*

```
function y=fuel(c0,a,b,p)
y=c0+a*p+b*p^2;                          %calculation gr/h


function IP = interPo(y0,y1,x0,x1,x)
IP=y0+(y1-y0)*((x-x0)/(x1-x0));          %interpolation
```

Figure A.5: *Support functions to calculation of SFOC*

A.4 Model verification

Figure A.6 - A.9 depict general waveforms of the synchronous generator in steady state. Due to the diode bridge, these waveforms distinct from conventional operation of a synchronous generator in an AC-grid. Simulations are performed with one generator online and load at $1\,pu$.

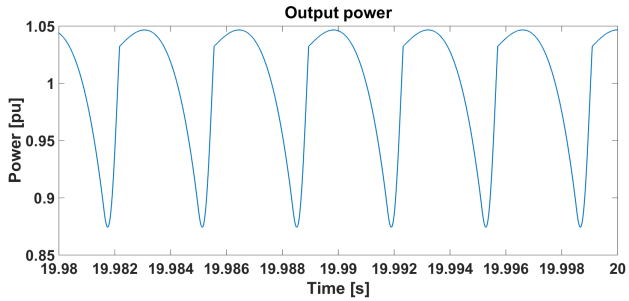

Figure A.6: *Output power of generator*

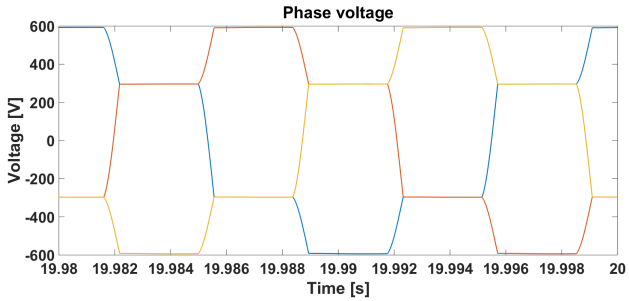

Figure A.7: *Phase to ground voltage of generator*

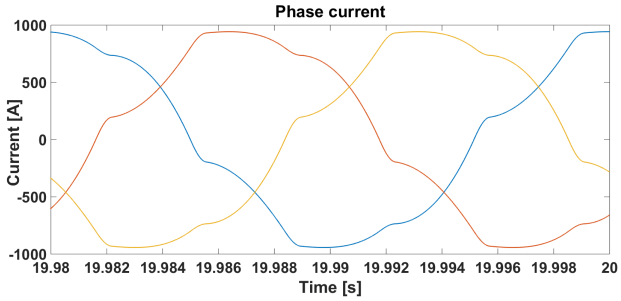

Figure A.8: *Phase-currents of generator*

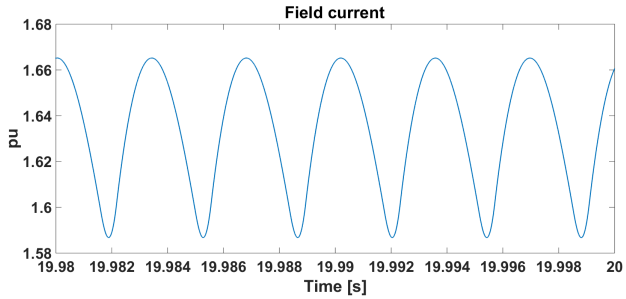

Figure A.9: *Field current of generator*

A.5 Tuning criteria of PI-controllers

In this thesis, several controllers are designed using PI-controllers. All the PI-controllers which are referred to, are one the form given in equation A.7. This section, briefly will explain two tuning criteria which often can be applied in many of the control cases in this thesis. These two strategies are called modulus optimum and symmetrical optimum. Which can be seen throughout this thesis, the designed controllers are not necessary tuned precisely with the design criteria of modulus and symmetric optimum. Rather control parameters are adapted to the actual system through simulations with these criteria used as a basis. Reference for tuning with modulus optimum and symmetrical optimum is provided from [56, p. 103].

$$H(s) = K_p \frac{1 + T_i s}{T_i s} \tag{A.7}$$

A.5.1 Modulus optimum

Modulus optimum is applied for control cases with open-loop transfer function given in equation A.8. In this transfer function all the small time-constants are equated into a first-order function and summed up into T_{sum}. T_1 is the dominant time constant and is distinctively larger than T_{sum}.

$$H_{OL}(s) = K_p \frac{1 + T_i s}{T_i s} \cdot K_s \frac{1}{1 + T_{sum}} \cdot \frac{1}{1 + T_1 s} \tag{A.8}$$

The design criteria of modulus optimum yield

$$T_i = T_1 \qquad K_p = \frac{T_1}{2 K_s T_{sum}} \tag{A.9}$$

By setting $T_i = T_1$ the following closed loop transfer function of equation A.8 is obtained

$$H_{CL}(s) = \frac{1}{(\frac{T_1 T_{sum}}{K_p K_s})s^2 + \frac{T_1}{K_p K_s}s + 1} \tag{A.10}$$

With $K_p = \frac{T_1}{2K_s T_{sum}}$ inserted in equation A.10, the closed loop transfer function reduces to

$$H_{CL}(s) = \frac{1}{2T_{sum}^2 s^2 + 2T_{sum}s + 1} \tag{A.11}$$

A.5.2 Symmetrical optimum

The second tuning criteria, symmetrical optimum, is applied to systems containing an integrator as shown in equation A.12. As for modulus optimum, T_1 denotes the dominant time constant and T_{sum}, the sum of all minor time constants.

$$H_{OL}(s) = K_p \frac{1 + T_i s}{T_i s} K_s \frac{1}{1 + T_{sum}s} \cdot \frac{1}{T_1 s} \tag{A.12}$$

The design criteria of symmetrical optimum are given in equation A.13. The term β can be adapted according to desired physical response.

$$T_i = \beta T_{sum} \qquad K_p = \frac{T_1}{2K_s T_{sum}\sqrt{\beta}} \tag{A.13}$$

B | Derivation of mathematical expressions

B.1 Transfer-functions DC-grid

The transfer-functions of $\frac{V_{DC}}{v_t}(s)$ and $\frac{I_{DC}}{v_t}(s)$ will be calculated in this section. For this purpose the equivalent circuit of the DC-grid is expressed in the s-plane as shown in figure B.1

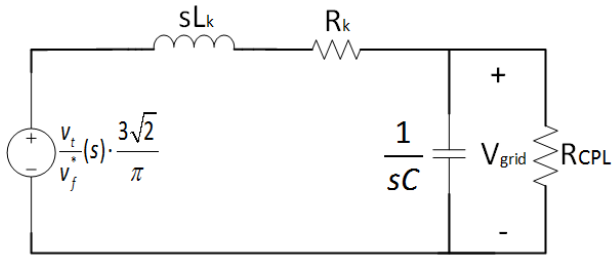

Figure B.1: *Equivalent DC-circuit of generator set defined in the s-plane*

From the equivalent circuit the impedance Z_{CR} is defined as

$$Z_{CR} = Cs||R_{CPL} = \frac{1}{Cs + \frac{1}{R_{CPL}}} = \frac{R_{CPL}}{R_{CPL}Cs + 1} \tag{B.1}$$

The total impedance Z_{tot} becomes

$$Z_{tot} = R_k + L_k + Z_{CR} \tag{B.2}$$

$$= R_k + sL_k + \frac{R_{CPL}}{R_{CPL}Cs + 1} \tag{B.3}$$

$$= \frac{(R_{CPL}Cs + 1)(R_k + sL_k) + R_{CPL}}{R_{CPL}C + 1} \tag{B.4}$$

$$= \frac{s^2(R_{CPL}L_kC) + s(R_{CPL}R_k + L_k) + R_k + R_{CPL}}{R_{CPL}Cs + 1} \tag{B.5}$$

$$= \frac{s^2\frac{R_{CPL}CL_k}{R_k+R_{CPL}} + s\frac{R_{CPL}R_k+L_k}{CR_k+R_{CPL}} + 1}{\frac{R_{CPL}Cs+1}{R_k+R_{CPL}}} \tag{B.6}$$

From the expressions of Z_{RC} and Z_{tot}, $\frac{V_{DC}}{v_t}(s)$ is obtained by voltatage dividing.

$$V_{DC} = v_t \cdot \frac{Z_{RC}}{Z_{tot}} \tag{B.7}$$

$$\frac{V_{DC}}{v_t}(s) = \frac{3\sqrt{2}}{\pi} \frac{\frac{R_{CPL}Cs+1}{R_k+R_{CPL}}}{s^2 \frac{R_{CPL}CL_k}{R_k+R_{CPL}} + s\frac{R_{CPL}R_k+L_k}{CR_k+R_{CPL}} + 1} \cdot \frac{R_{CPL}}{R_{CPL}Cs+1} \tag{B.8}$$

$$= \frac{3\sqrt{2}}{\pi} \frac{\frac{R_{CPL}}{R_{CPL}+R_k}}{s^2 \frac{R_{CPL}CL_k}{R_{CPL}+R_k} + s\frac{CR_kR_{CPL}+L_k}{R_{CPL}+R_k} + 1} \tag{B.9}$$

The expression of $\frac{I_{DC}}{v_t}(s)$ is obtained by the terminal voltage divided by the total impedance.

$$i_{DC}(s) = \frac{v_t(s)\frac{3\sqrt{2}}{\pi}}{Z_{tot}} \tag{B.10}$$

$$\frac{i_{DC}}{v_t}(s) = \frac{3\sqrt{2}}{\pi} \frac{\frac{R_{CPL}Cs+1}{R_k+R_{CPL}}}{s^2 \frac{R_{CPL}CL_k}{R_k+R_{CPL}} + s\frac{R_{CPL}R_k+L_k}{CR_k+R_{CPL}} + 1} \tag{B.11}$$

B.2 Expressions droop-control

The power share of power units by using droop controller is derived in this section. First the power share of between two generator sets operating alone is derived. Next, the power share of two generator sets with the battery is derived.

For the two generator sets and the battery, the droop function respectively yields

$$V_{DC}^* = V_{01} - \delta_1 P_{gen1} \tag{B.12}$$

$$V_{DC}^* = V_{02} - \delta_2 P_{gen2} \tag{B.13}$$

$$V_{DC}^* = V_{0,bat} - \delta_{bat} P_{bat} \tag{B.14}$$

Two generator sets alone

When two generator sets are operating, the total power supplied to the DC-link is

$$P_{tot} = P_{gen1} + P_{gen2} \tag{B.15}$$

As the reference voltage to each generator will be equal equation B.12 and B.13 can be set equal

$$V_{DC}^* = V_{01} - \delta_1 P_{gen1} = V_{02} - \delta_2 P_{gen2} \tag{B.16}$$

From equation B.15, the power of generator set 2 can be expressed in terms of generator set 1

$$P_{gen2} = P_{tot} - P_{gen1} \tag{B.17}$$

Inserting equation B.17 into B.16 yields

$$V_{01} - \delta_1(P_{tot} - P_{gen2}) = V_{02} - \delta_2 P_{gen2} \tag{B.18}$$

Rearranging yields

$$P_{gen2}(\delta_2 + \delta_1) = V_{02} - V_{01} + \delta_1 P_{tot} \tag{B.19}$$

$$P_{gen2} = \frac{V_{02} - V_{01} + \delta_1 P_{tot}}{\delta_2 + \delta_1} \tag{B.20}$$

From the calculation of P_{gen2}, P_{gen1} can be obtained by

$$\underline{P_{gen1} = P_{tot} - P_{gen2}} \tag{B.21}$$

Two generator sets and battery

As the reference voltage for each power unit is the same, equation B.12- B.14, can be applied to set up the following expression

$$V_{01} - \delta_1 P_{gen1} = V_{02} - \delta_2 P_{gen2} \tag{B.22}$$

$$V_{02} - \delta_2 P_{gen2} = V_{0,bat} - \delta_{bat} P_{bat} \tag{B.23}$$

The power balance between the battery and generator sets becomes

$$P_{tot} = P_{gen1} + P_{gen2} + P_{bat} \tag{B.24}$$

Rearranging equation B.22-B.24 with respect to the the variables P_{gen1}, P_{gen2} and P_{bat} on the left side and the constants V_{01}, V_{02}, $V_{0,bat}$ and P_{tot} on the right side, equation B.25-B.27 can be obtained. These three equations comprises an equations set, that can be resolved in a matrix set up.

$$-P_{gen1}\delta_1 - P_{gen2}\delta_2 = V_{01} - V_{02} \tag{B.25}$$

$$P_{gen2}\delta_2 - P_{Bat}\delta_{bat} = V_{02} - V_{0,bat} \tag{B.26}$$

$$P_{gen1} + P_{gen2} + P_{bat} = P_{tot} \tag{B.27}$$